

# Description of seismic sources in underground mines: Dynamic stress fracturing around tunnels and strainbursting

Dmitriy Malovichko & Alex Rigby

May 17, 2022

Institute of Mine Seismology, 10 Church Street, Kingston, 7050, Australia

## Abstract

This paper considers the dynamic fracturing of the rockmass surrounding a tunnel statically loaded by compressional stress as a possible source of seismic events in underground mines. This begins with two-dimensional dynamic modelling of failure for six plausible scenarios that span various loadings, tunnel profiles, rockmass parameters, and methods of event initiation. In each case, the seismic source derived from these models has significant negative isotropic (implosive) and negative compensated linear vector dipole (pancake-shape) components as well as a P-axis that is approximately aligned with the direction of maximum compressional principal stress. These features indicate that at wavelengths larger than the diameter of the tunnel and the extent of damage along it, seismic radiation is controlled by the elastic convergence of the surrounding rockmass rather than by rock fracturing. To aid in the analysis of such events, an analytical approximation of the source mechanism is suggested [Equation (3)] that is based solely on mechanical and geometric properties: the magnitudes  $\sigma_{\max}$  and  $\sigma_{\min}$  of the maximum and minimum principal stresses orthogonal to the tunnel's axis, the Poisson's ratio  $\nu$  of the rockmass, the length  $L_3$  of dynamic fracturing along the tunnel, the effective tunnel dimension  $\overline{L}_A$ , and the increase in depth of failure  $\Delta d_f^A$  in the direction of  $\sigma_{\min}$ . Furthermore, it is shown that the scalar seismic moment can be approximated as  $|\mathbf{M}| \approx 2[(1 - \nu)/(1 - 2\nu)] |\sigma_{\max}| L_3 \overline{L}_A \Delta d_f^A$ . The suggested approximations are considered in the context of seismic data from a real underground mine. It is shown that many mechanisms inverted from observed waveforms are consistent with the suggested model. Furthermore, it is demonstrated that the proposed source mechanism approximation can be used for the forensic analysis of damaging seismic events and quantitative monitoring of the evolution of fractured zones around tunnels.

## 1 Introduction

In mines, episodes of sudden inelastic deformation are often induced or triggered by the excavation of rocks, with examples including slip along a fault adjacent to a mined-out stope or the failure of a pillar between two tunnels. As discussed in [19], these nearby excavations can have a significant effect on the radiation of seismic waves and should be taken into account in the elastodynamic Green's function adopted in the modelling or inversion of waveforms. An alternative approach is to consider the excavations as part of the seismic source. Expressions describing such point sources are suggested in [19] and are appropriate when seismic wavelengths exceed the combined size of the volume of sudden inelastic deformation and nearby excavations.

The focus of this paper is the application of these expressions to a particular type of dynamic process in underground mines: violent stress fracturing around tunnels. If this process results in observable damage to the excavation (as is shown in Figure 1), then it is referred to as a strainburst. Strainbursts are of great concern in the mining industry as they compromise safety and disrupt production plans. Typically, instances of violent damage to excavations are thoroughly investigated to identify causes and contributing

factors. Such forensic investigations can be aided by the use of seismic data, whether it be the waveforms of the seismic event associated with the strainburst or a catalog of seismic events recorded around the strainburst's location. Note that dynamic stress fracturing around a tunnel need not be accompanied by damage to excavations: the ground support system (rock bolts, mesh, shotcrete, etc.) may accommodate the deformation of fractured rock and prevent damage. Even in such cases, the fracturing process can be intensive and fast enough to radiate detectable seismic waves, and the analysis of these signals is beneficial from the perspective of understanding the deformation around tunnels and the assessment of consumption of ground support capacity.

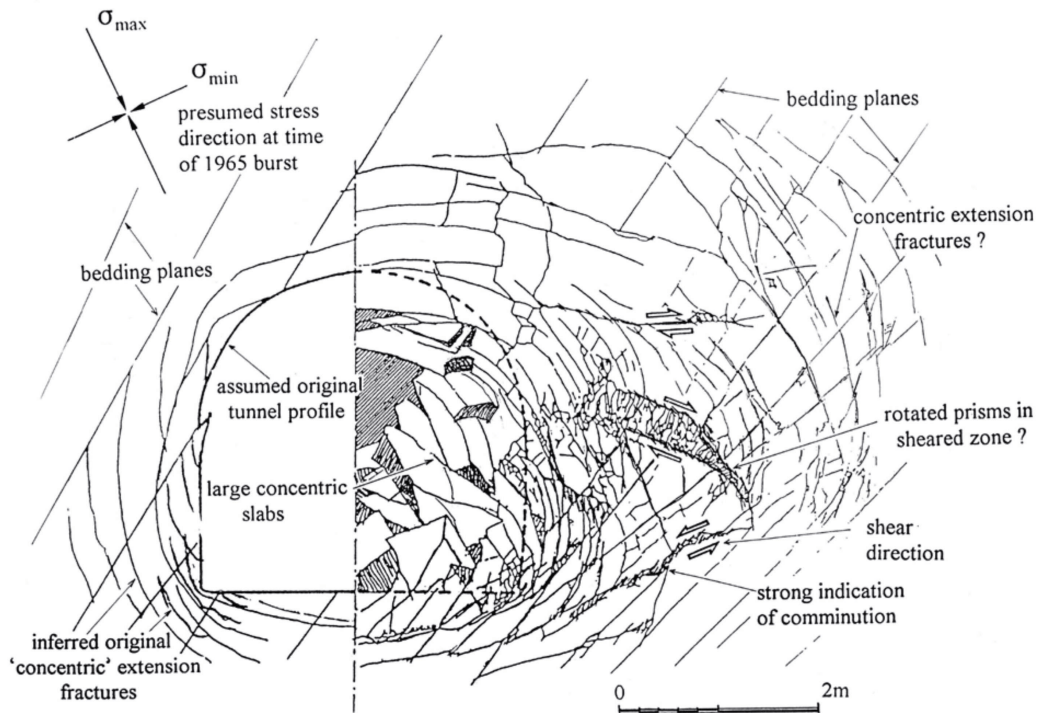


Figure 1: Interpretation of fracturing around a rockburst-damaged tunnel in a deep gold mine in South Africa [25]. The left half of the sketch describes conditions expected to exist before the rockburst, and the right half was drawn based on a photograph of damage.

As is shown in Figure 1, the overall process of dynamic stress fracturing may be decomposed into smaller-scale episodes of shear or tensile rupturing of the rockmass, the seismic radiation of which can be approximately described by conventional double-couple or tensile-crack point sources (although modelling the medium as unbounded space may not be appropriate [29]). Given the potentially sub-meter length scales of these constituent processes, observation of the radiated waves would require a dense seismic array consisting of acoustic emission sensors capable of recording in the multi-kHz frequency range. However, typical seismic systems in underground mines have sparse arrays of sensors adequate for the recording of signals with wavelengths on the order of tens or hundreds of meters. Such waves do not provide enough resolution to distinguish the details of fracturing as shown in Figure 1, and only the overall pattern of fracturing can be inferred. In such a case, it is convenient to consider the tunnel as part of the seismic source, which makes it possible to utilize a simple elastodynamic Green's function for homogeneous, isotropic space that does not take the presence of the tunnel into account.

To the best knowledge of the authors, there are no established quantitative point-source models describing the low-frequency content of seismic radiation produced by strainbursts (or dynamic stress fracturing around excavations in general). However, some characteristics of such sources have been postulated. For example, [25] states that strainbursts have an implosive seismic signature (first motion towards

the source from the seismic records) and a local magnitude ranging from  $-0.2$  to  $0.0$ . In [21], an example of a seismic event is considered whose source presumably involves the closure of an excavation (stope). It is suggested that the isotropic component of the moment tensor  $M_{ij}$  for such events can be interpreted in terms of a coseismic volumetric change  $\Delta V = \text{tr}(M_{ij})/(3\lambda + 2\mu)$ , where  $\lambda$  and  $\mu$  are the Lamé moduli for the rockmass. This interpretation is based on Equation (3.35) of [1], which describes the transformational expansion (or contraction) of a spherical volume in an isotropic medium.

Seismic sources associated with inelastic deformation around tunnels were briefly considered in a previous work [19], where two simple cases were analyzed. In the first case, a circular tunnel in an elastic-brittle-plastic Mohr-Coulomb material was loaded hydrostatically. Analytical solutions for stress and displacement [8] were then used to evaluate a corresponding seismic source mechanism that took the effect of the tunnel into account. This mechanism had a significant isotropic implosive component and a deviatoric component in the form of a negative (largest dipole compressional) compensated linear vector dipole (CLVD), which is hereafter referred to as a “pancake-shape” CLVD. The second case considered was the nonhydrostatic loading of a rectangular tunnel. In the absence of analytical expressions for stress and displacement, a finite-difference analysis was performed. This involved modelling deformation of limited extent along the tunnel’s axis on two of its sides. Again, the corresponding seismic source mechanism, which accounted for the tunnel, consisted mainly of implosive and pancake-shape CLVD components.

In this paper, we first extend these previous results in Section 2, where six cases of nonhydrostatically loaded two-dimensional tunnels are considered that differ in loading, tunnel profile, rockmass parameters, and method of event initiation. For each of these cases, numerical modelling of deformation around the tunnel is performed. Using these modelling results, two different approaches to calculating seismic mechanisms are outlined, and the main features of these mechanisms are discussed. While such modelling can be a useful instrument in the forensic analysis of strainbursts, such an approach may not always be computationally feasible. To address this limitation, Section 3 suggests an analytical approximation that provides a quantitative relation between the geometric and mechanical characteristics of the fracturing process around a tunnel (tunnel dimension, properties of loading, etc.) and the parameters of an equivalent seismic point source (mechanism and scalar moment). This approximate model is verified against the results of Section 2, with a good agreement between the two approaches being demonstrated. Section 4 presents examples of real data that can be interpreted in terms of the discussed source model and its suggested approximation. The paper is concluded in Section 5.

## 2 Numerical modelling of sources

### 2.1 Conceptual overview

In this section and Section 3, we consider horizontal tunnels, like the one shown in Figure 2, that are located in a homogeneous rockmass with no other nearby excavations. For notational simplicity, we take these tunnels to be north-south oriented. Nonhydrostatic loading is considered, with maximum compressional stress orthogonal to the tunnel being either horizontal, vertical, or plunging to the east (as is depicted in Figure 2). In the latter case, such loading facilitates rockmass damage in the eastern shoulder (upper corner) and bottom western corner of the tunnel as shown in yellow in Figure 2.

Suppose that some process (for example, a slow increase in loading, the stress wave from a distant blast, etc.) triggers dynamic fracturing, which can be described as an expansion of the damaged zone (shown in red in Figure 2). This will typically be accompanied by a bulking of the rockmass (increase of volume due to geometrical inconsistencies of rock fragments) and its overall movement into the excavation. If the described processes of fracturing and convergence occur suddenly (within a fraction of a second), then this can result in the radiation of seismic waves through the surrounding elastic zone. These waves can be strong enough to be detected by seismic sensors that are typically used for the monitoring of underground mines. As such, the considered process constitutes the source of a seismic event.

The sudden unidirectional deformation of the rockmass moving into the excavation contributes to

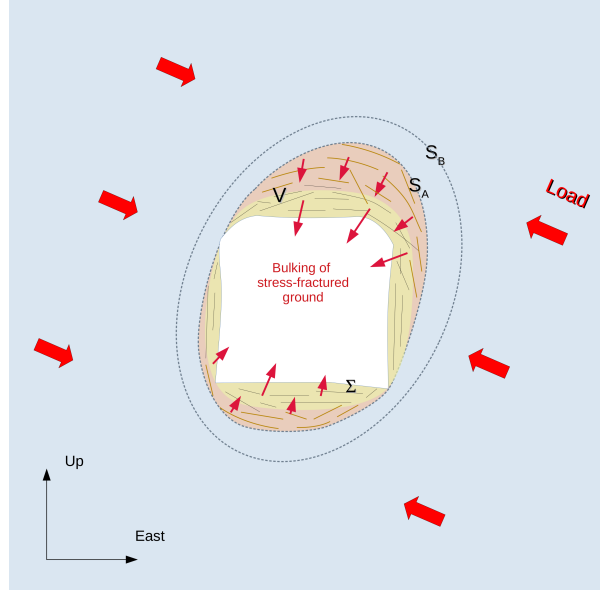


Figure 2: A conceptual model of fracturing around a tunnel. It is assumed that the growth of damage zone from yellow to red happens suddenly (within a fraction of second). Several geometrical characteristics used in the calculation of seismic source parameters are marked: the volume  $V$  containing damaged rock, the tunnel surface  $\Sigma$ , the external boundary  $S_A$  of damaged rock, and a surface  $S_B$  enclosing both the tunnel and the damaged region.

seismic radiation and can be described by a single-force point source [33]. While this contribution to total radiation is expected to be minor, proper quantification is required and deserves a separate study. The major portion of radiation is anticipated to come from the next term in the polynomial decomposition of equivalent forces: the seismic moment tensor (or, more correctly, the stress glut tensor) [2]. This tensor's components can be calculated using either the Kirchhoff-type or adjusted conventional expressions suggested in [19]:

$$M_{ij} = M_{ij}^T + M_{ij}^U = \iint_S \Delta T_i(\mathbf{x})(x_j - x_j^{(0)}) dS(\mathbf{x}) - \iint_S c_{ijkl}(\mathbf{x}) \Delta u_k(\mathbf{x}) n_l(\mathbf{x}) dS(\mathbf{x}), \quad (1)$$

$$M_{ij} = M_{ij}^e + M_{ij}^u = \iiint_V c_{ijkl}(\mathbf{x}) \Delta e_{kl}(\mathbf{x}) dV(\mathbf{x}) - \iint_\Sigma c_{ijkl}(\mathbf{x}) \Delta u_k(\mathbf{x}) n_l(\mathbf{x}) d\Sigma(\mathbf{x}), \quad (2)$$

where  $\Delta \mathbf{T} = \mathbf{T}^{(\text{after})} - \mathbf{T}^{(\text{before})}$  and  $\Delta \mathbf{u} = \mathbf{u}^{(\text{after})} - \mathbf{u}^{(\text{before})}$  are the differences in traction and displacement, respectively, before and after expansion of the damaged region to volume  $V$ ,  $\Delta \mathbf{e}$  is the stress-free strain tensor,  $S$  is a surface in the elastic region enclosing the damage,  $\Sigma$  is the tunnel's surface,  $\mathbf{x}^{(0)}$  is an arbitrary point,  $\mathbf{n}$  is an inward unit normal to  $\Sigma$  or  $S$ , and  $c_{ijkl}$  is the stiffness tensor. For an isotropic medium,  $c_{ijkl} = \lambda \delta_{ij} \delta_{kl} + \mu (\delta_{ik} \delta_{jl} + \delta_{il} \delta_{jk})$ , where  $\delta_{ij}$  is the Kronecker delta function. The stress-free strain is mathematically equivalent to the increment of plastic strain  $\Delta \boldsymbol{\epsilon}^p$  according to the theory of plastic flow [17].  $\Sigma$ ,  $V$ , and two possible selections of the surface  $S$  are shown in Figure 2. As discussed in [19], the dimension of  $S$  must be kept smaller than the wavelengths of interest, meaning that it must cut through the tunnel to the north and south of the extent of damage in this case (this is valid provided the excluded parts of the excavation experience small displacements during the period of inelastic deformation of  $V$ ).

Each of the stated expressions is split naturally into two terms: the first into traction  $\mathbf{M}^T$  and displacement  $\mathbf{M}^U$  components, and the second into strain  $\mathbf{M}^e$  and displacement  $\mathbf{M}^u$  components. The contribution of these terms to the total mechanism will be compared using the conventional norm  $|\mathbf{M}| =$



$\sum_{ij} \sqrt{M_{ij}^2/2}$  defining a scalar moment [30]. Note that while  $|\mathbf{M}^e + \mathbf{M}^u| \leq |\mathbf{M}^e| + |\mathbf{M}^u|$  and  $|\mathbf{M}^e + \mathbf{M}^u| \leq |\mathbf{M}^e| + |\mathbf{M}^u|$ , equality need not hold in either case.

## 2.2 Cases

As depicted in Figure 3, six cases based on the general setup described in Subsection 2.1 are considered in this paper. To simplify analysis, we approximate the dynamic stress fracturing along a finite extent of a tunnel by considering a finite-length ( $L_3 = 5$  m) slice of an infinite-length tunnel (oriented north-south), which reduces the problem to two dimensions under the assumption of plane strain. The tunnel cross section has both a height and width of 5 m, square bottom corners and rounded shoulders; for Cases 1-4 and 6 the radius of curvature of this rounding is  $R = 2.5$  m (that is, the top half of the tunnel is circular), while for Case 5, we take  $R = 1.25$  m (resulting in a geometry similar to that shown in Figure 2).

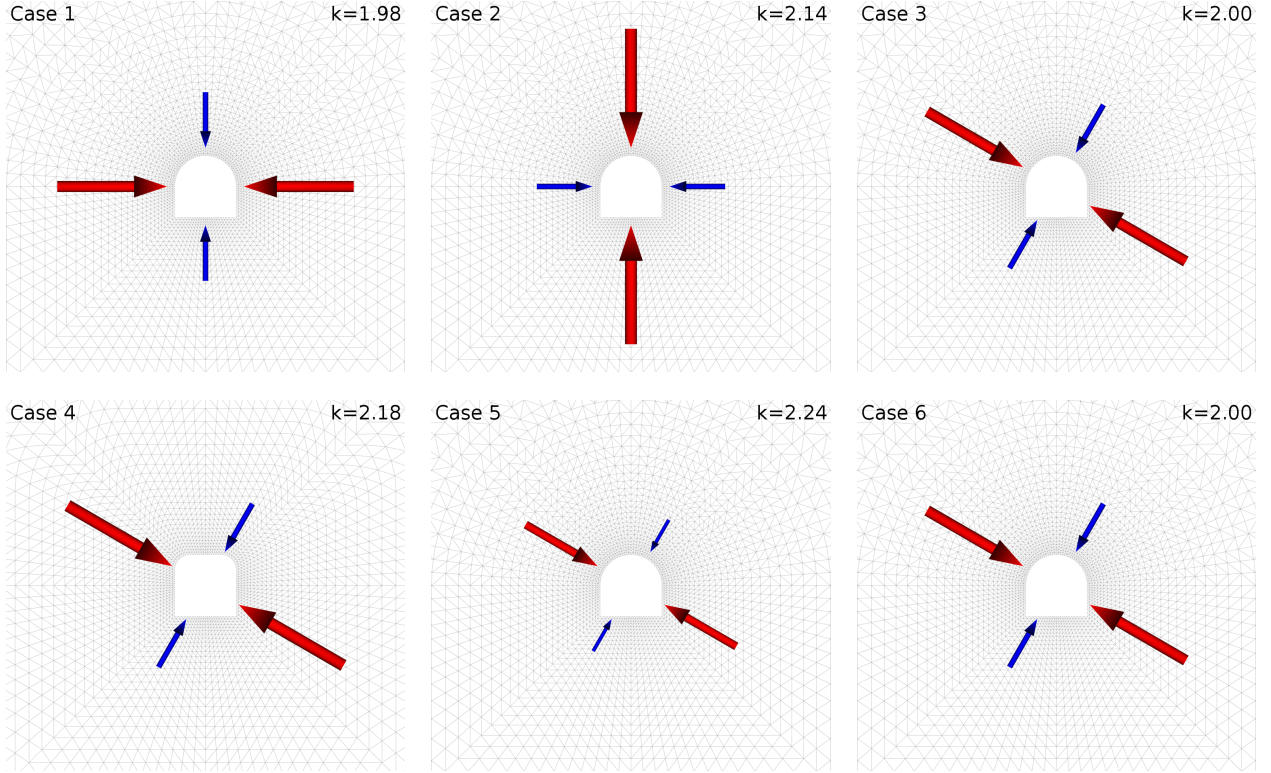


Figure 3: Graphical summary of the six cases outlined in Subsection 2.2. The arrows show the orientation of the maximum (red) and minimum (blue) in-plane loading, the ratio of which is listed in the top right.

As noted in Subsection 2.1, nonhydrostatic loading is considered. The minor in-plane loading is  $\sigma_{\min} = -20$  MPa for Case 5 and  $-30$  MPa for the remaining cases. Maximum in-plane loading is  $\sigma_{\max} = k\sigma_{\min}$ , where the stress ratio  $k$  for each case can be found in Figure 3. Major loading is horizontal for Case 1, vertical for Case 2, and plunging  $30^\circ$  to the east for the remaining cases.

A cohesion-weakening-friction-strengthening (CWFS) material [9, 7] is used for all cases. Details of implementation and verification of this constitutive model are outlined in Appendix A. In all cases, the Lamé moduli defining the material's elastic behavior are  $\mu = \lambda = 30$  GPa (giving a Poisson's ratio of  $\nu = 0.25$ ). For Cases 1-4 and 6, the material has friction angle  $\phi = 25^\circ$ , cohesion  $c = 50$  MPa, residual friction angle  $\phi_r = 50^\circ$ , residual cohesion  $c_r = 2$  MPa, dilation angle  $\psi = 20^\circ$ , tensile strength  $\sigma_t = 8$  MPa, and a deviatoric plastic strain limit  $\varepsilon_c^p = \varepsilon_\phi^p = 3 \times 10^{-3}$ . For Case 5, a weaker material is used with  $\phi = 15^\circ$ ,  $c = 30$  MPa,  $\phi_r = 50^\circ$ ,  $c_r = 2$  MPa,  $\sigma_t = 5$  MPa, and  $\varepsilon_c^p = \varepsilon_\phi^p = 3 \times 10^{-3}$ .

After reaching equilibrium with the loading and material properties as described above, expansion of the failure region is triggered by slowly increasing the stress ratio by  $\Delta k = 0.01$  for Cases 1-5. This serves to replicate slow loading of the tunnel by nearby mining. For Case 6, expansion is induced by dynamically loading the tunnel with a stress wave. In particular, a half-sine pulse of force density directed vertically is applied in a  $30 \times 5$  m region centered 20 m beneath the tunnel with a period of 0.01 s and amplitude of  $10^6 \text{ N} \cdot \text{m}^{-3}$  (this results in a peak ground velocity of approximately  $0.2 \text{ ms}^{-1}$ ).

## 2.3 Results

Dynamic simulation of the outlined cases was performed using the Material Point Method (MPM). The MPM implementation used [3] is based on the formulations of [23, 15]. Verification across a number of relevant cases for which analytical solutions are available has been undertaken and is documented in the supplemental material. In an MPM simulation, the domain of interest is discretized as Lagrangian material points, or particles, that interact with each other via the nodes of a Eulerian background grid (this allows for convenient handling of large deformations without remeshing). Given the plane strain assumption, this grid is based on a thin plate that is meshed by a single layer of tetrahedra. Details on the construction of this mesh, the initial and boundary conditions employed, and other aspects of the simulation process can be found in Appendix A. Animations showing the dynamics of the expansion of the failed region are included in the supplemental material.

Using Equations (1) and (2), it is possible to extract source mechanisms from the results of numerical modelling. We take Case 3 as an example of this procedure, which is represented graphically in Figure 4. The top left and middle plots show values and directions of traction  $\mathbf{T}$  and displacement  $\mathbf{u}$  on a surface  $S$  enclosing the damaged region before and after its expansion. The top right plot shows their differences ( $\Delta \mathbf{T}$  and  $\Delta \mathbf{u}$ , respectively), which are used in Equation (1) to calculate a seismic mechanism that is shown as a beachball (with the P-axis in red, B-axis in green, and T-axis in blue). The bottom left and middle plots depict plastic strain  $\epsilon^p$  and tunnel surface displacement  $\mathbf{u}$  before and after the expansion of the damaged region. Their differences ( $\Delta \epsilon^p$  and  $\Delta \mathbf{u}$ , respectively, shown in the bottom right) are then used in Equation (2) to determine the source mechanism shown. In the Kirchhoff case, the surface  $S$  was chosen to be composed from the north-south oriented faces lying on the contour shown in black; however, as shown in Appendices A and B for all cases, this selection does not affect the resulting moment (as long as the contour is sufficiently far from the external boundary of the modelling domain). Note that this surface does not enclose the damaged region in the north-south direction. This stems from our two-dimensional approach, which means that extending  $S$  to include faces on the north or south ends of the mesh would result in intersecting the damaged region. However, the results of this subsection will demonstrate that this compromise in surface selection does not result in significant deviation of the results of Equation (1) from those of Equation (2).

Figures showing the difference between the pre- and post-expansion states for all cases are given in Appendix A. To compare the source mechanisms obtained using Equations (1) and (2) for these cases, three main characteristics are summarized in Tables 1 and 2:

- Source size in terms of scalar seismic moment  $|\mathbf{M}|$  (expressed in  $\text{N} \cdot \text{m}$ ) and Hanks-Kanamori moment magnitude  $m_{\text{HK}} = 0.667 \log_{10} |\mathbf{M}| - 6.033$  [10] (Table 1).
- Signs and ratios of eigenvalues expressed in terms of  $k$  and  $T$  parameters as displayed in the source-type plot of [11] (middle column of Table 2).
- Orientations of principal axes as displayed in a lower-hemisphere stereonet plot (last column of Table 2).

The Kirchhoff-type [Equation (1)] and adjusted conventional [Equation (2)] expressions provide similar results with regard to sizes and orientation of principal P axes: the difference in moment magnitude  $m_{\text{HK}}$  does not exceed 0.02 and the difference in the directions of principal axes is within  $1^\circ$ . Furthermore, the

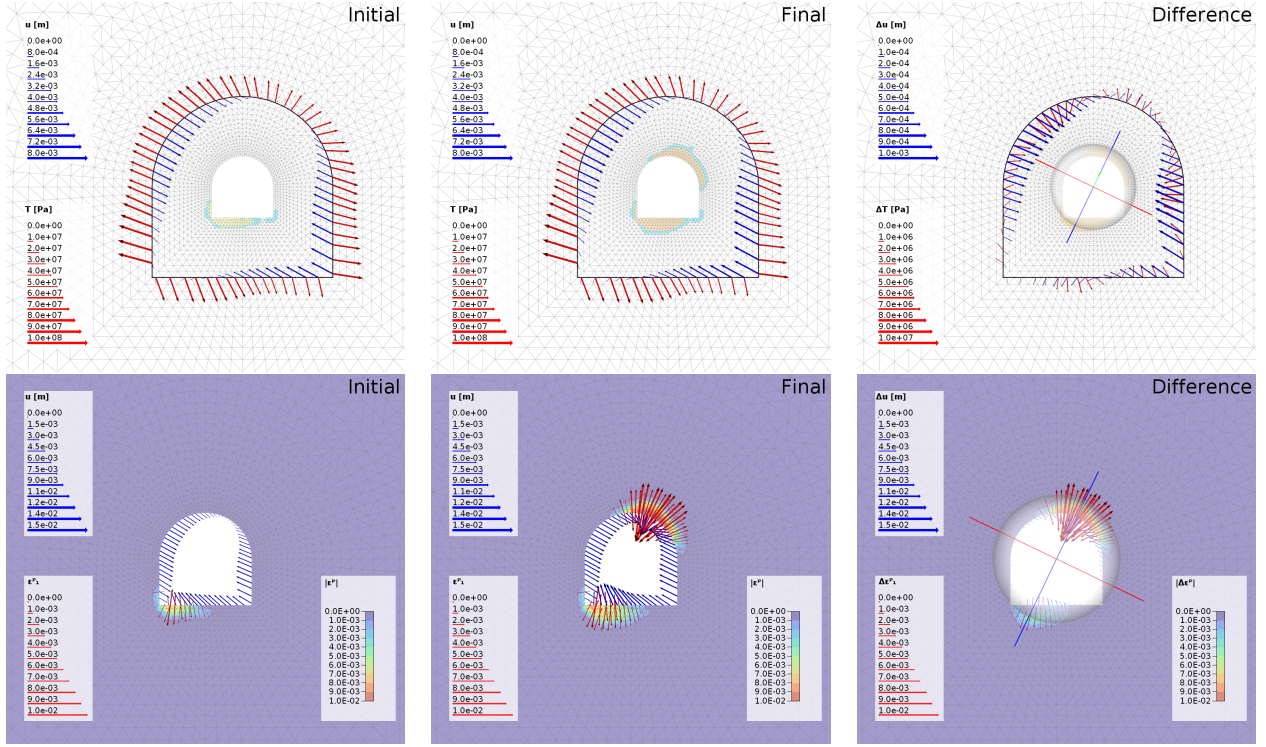


Figure 4: Illustration of the inputs in seismic mechanism calculation for Case 3 using Equations (1) and (2). Also shown are the resulting mechanisms as beachballs (P-axis in red, B-axis in green, and T-axis in blue). Descriptions are provided in the text.

source types are similar with respect to the sign and size of their isotropic components, with the difference in  $k$  parameter between Kirchhoff-type and adjusted conventional solutions being less than 0.03. There is a larger disparity in the  $T$  parameter (which measures the deviation of the deviatoric component from a double-couple model); the largest such difference being 0.36 for Case 3. However, we note that the region of the source plot corresponding to significant CLVD and isotropic components ( $T$  above 0.6 and  $k$  below  $-0.4$ ) has a high density of isolines of constant  $T$ , which indicates that this seemingly substantial difference in the  $T$  parameter is not necessarily translated to a significant difference in other metrics (such as the angle  $\omega$  explained in Section 5). The difference in  $T$  parameter values may be an artifact of the previously discussed compromises made in the selection of integration surface for the Kirchhoff-type expression. The similarity in B- and T-axis eigenvalues for sources of this type also results in their orientations not being well constrained. This can be seen for Case 6, where these axes are interchanged for the two methods of moment tensor calculation.

Overall, the sources derived from modelling have significant negative isotropic (implosive) and negative compensated linear vector dipole (pancake-shape) components as well as a P-axis that is aligned with the direction of maximum compressional principal stress. These features indicate that at wavelengths larger than the diameter of the tunnel and the extent of the damage along it, seismic radiation is controlled by the elastic convergence of the surrounding rockmass rather than by rock fracturing (which is explosive when considered in isolation). Furthermore, there is not a strong dependence of the method of triggering on the resulting source. This is evidenced by the similarity between the seismic mechanisms for Cases 3 and 6, which differ only in the method of triggering (quasi-static load increase and transient stress wave, respectively).

Table 1: Comparison of the the modelled source mechanisms in terms of scalar moment  $|\mathbf{M}|$  and Hanks–Kanamori moment magnitude  $m_{\text{HK}}$ . The listed variants are:  $K$ – Kirchhoff-type expression [Equation (1)],  $K - T$  – Kirchhoff-type expression traction term,  $K - D$  – Kirchhoff-type expression displacement term,  $C$  – adjusted conventional expression [Equation (2)],  $C - S$  – adjusted conventional expression strain term,  $C - D$  – adjusted conventional expression displacement term,  $N$  – numerically evaluated expression for the elliptical cavity described in Subsection 3.2,  $N - T$  – numerical expression traction term,  $N - D$  – numerical expression displacement term,  $A$  – analytical approximation for the effective elliptical cavity described in Subsection 3.3,  $|C_M|$  – simple approximations of the  $A$  case. The “ $|\mathbf{M}|$  ratio” rows list moments normalized to the Kirchhoff-type moment  $K$ . The  $\Delta m_{\text{HK}}$  rows list difference in moment magnitude compared to the Kirchhoff-type moment  $K$ . Traction and displacement terms for Kirchhoff-type and numerical expressions have been calculated for 15 m diameter contours.

Case	Parameter	$K$	$K - T$	$K - D$	$C$	$C - S$	$C - D$	$N$	$N - T$	$N - D$	$A$	$ C_M $
1	$ \mathbf{M} $ [ $10^9 \text{N} \cdot \text{m}$ ]	<b>8.55</b>	2.62	6.01	<b>8.19</b>	12.13	15.41	<b>11.17</b>	3.70	7.58	<b>11.43</b>	<b>12.22</b>
	$m_{\text{HK}}$	<b>0.59</b>	0.25	0.49	<b>0.58</b>	0.69	0.76	<b>0.67</b>	0.35	0.55	<b>0.67</b>	<b>0.69</b>
	$ \mathbf{M} $ ratio	-	-	-	<b>0.96</b>	-	-	<b>1.31</b>	-	-	<b>1.34</b>	<b>1.43</b>
	$\Delta m_{\text{HK}}$	-	-	-	<b>-0.01</b>	-	-	<b>0.08</b>	-	-	<b>0.08</b>	<b>0.10</b>
2	$ \mathbf{M} $ [ $10^9 \text{N} \cdot \text{m}$ ]	<b>8.06</b>	2.39	5.75	<b>7.82</b>	11.42	15.01	<b>9.86</b>	3.20	6.76	<b>9.72</b>	<b>10.10</b>
	$m_{\text{HK}}$	<b>0.57</b>	0.22	0.47	<b>0.56</b>	0.67	0.75	<b>0.63</b>	0.30	0.52	<b>0.63</b>	<b>0.64</b>
	$ \mathbf{M} $ ratio	-	-	-	<b>0.97</b>	-	-	<b>1.22</b>	-	-	<b>1.21</b>	<b>1.25</b>
	$\Delta m_{\text{HK}}$	-	-	-	<b>-0.01</b>	-	-	<b>0.06</b>	-	-	<b>0.05</b>	<b>0.07</b>
3	$ \mathbf{M} $ [ $10^9 \text{N} \cdot \text{m}$ ]	<b>4.69</b>	1.34	3.39	<b>4.33</b>	5.02	7.36	<b>5.62</b>	1.85	3.83	<b>5.79</b>	<b>6.12</b>
	$m_{\text{HK}}$	<b>0.41</b>	0.05	0.32	<b>0.39</b>	0.43	0.55	<b>0.47</b>	0.14	0.36	<b>0.48</b>	<b>0.49</b>
	$ \mathbf{M} $ ratio	-	-	-	<b>0.92</b>	-	-	<b>1.20</b>	-	-	<b>1.23</b>	<b>1.30</b>
	$\Delta m_{\text{HK}}$	-	-	-	<b>-0.02</b>	-	-	<b>0.05</b>	-	-	<b>0.06</b>	<b>0.08</b>
4	$ \mathbf{M} $ [ $10^9 \text{N} \cdot \text{m}$ ]	<b>1.91</b>	0.41	1.51	<b>1.87</b>	2.49	3.33	<b>2.42</b>	0.79	1.66	<b>2.66</b>	<b>2.83</b>
	$m_{\text{HK}}$	<b>0.15</b>	-0.29	0.09	<b>0.15</b>	0.23	0.32	<b>0.22</b>	-0.10	0.11	<b>0.25</b>	<b>0.27</b>
	$ \mathbf{M} $ ratio	-	-	-	<b>0.98</b>	-	-	<b>1.27</b>	-	-	<b>1.40</b>	<b>1.48</b>
	$\Delta m_{\text{HK}}$	-	-	-	<b>-0.01</b>	-	-	<b>0.07</b>	-	-	<b>0.10</b>	<b>0.11</b>
5	$ \mathbf{M} $ [ $10^9 \text{N} \cdot \text{m}$ ]	<b>1.23</b>	0.31	0.93	<b>1.18</b>	1.18	1.74	<b>1.73</b>	0.58	1.16	<b>1.64</b>	<b>1.66</b>
	$m_{\text{HK}}$	<b>0.03</b>	-0.37	-0.05	<b>0.02</b>	0.01	0.13	<b>0.13</b>	-0.19	0.01	<b>0.11</b>	<b>0.11</b>
	$ \mathbf{M} $ ratio	-	-	-	<b>0.96</b>	-	-	<b>1.41</b>	-	-	<b>1.34</b>	<b>1.35</b>
	$\Delta m_{\text{HK}}$	-	-	-	<b>-0.01</b>	-	-	<b>0.10</b>	-	-	<b>0.08</b>	<b>0.09</b>
6	$ \mathbf{M} $ [ $10^9 \text{N} \cdot \text{m}$ ]	<b>4.54</b>	1.56	3.02	<b>4.20</b>	5.05	7.43	<b>5.75</b>	1.89	3.92	<b>5.97</b>	<b>6.19</b>
	$m_{\text{HK}}$	<b>0.40</b>	0.10	0.29	<b>0.38</b>	0.44	0.55	<b>0.47</b>	0.15	0.36	<b>0.48</b>	<b>0.49</b>
	$ \mathbf{M} $ ratio	-	-	-	<b>0.93</b>	-	-	<b>1.27</b>	-	-	<b>1.32</b>	<b>1.36</b>
	$\Delta m_{\text{HK}}$	-	-	-	<b>-0.02</b>	-	-	<b>0.07</b>	-	-	<b>0.08</b>	<b>0.09</b>



Table 2: Source mechanism characteristics for modelled Cases 1-6. Mechanisms are shown in source-type plots of [11] and in lower-hemisphere stereonet plots. The labels describe the procedure used to calculate the mechanism:  $K$  – Kirchhoff-type expression [Equation (1)],  $C$  – adjusted conventional expression [Equation (2)],  $N$  – numerically evaluated expression for the elliptical cavity described in Subsection 3.2,  $A$  – analytical approximation for the effective elliptical cavity described in Subsection 3.3. The overlays in the source-type plots describing different sources are explained in Subsection 5.1.

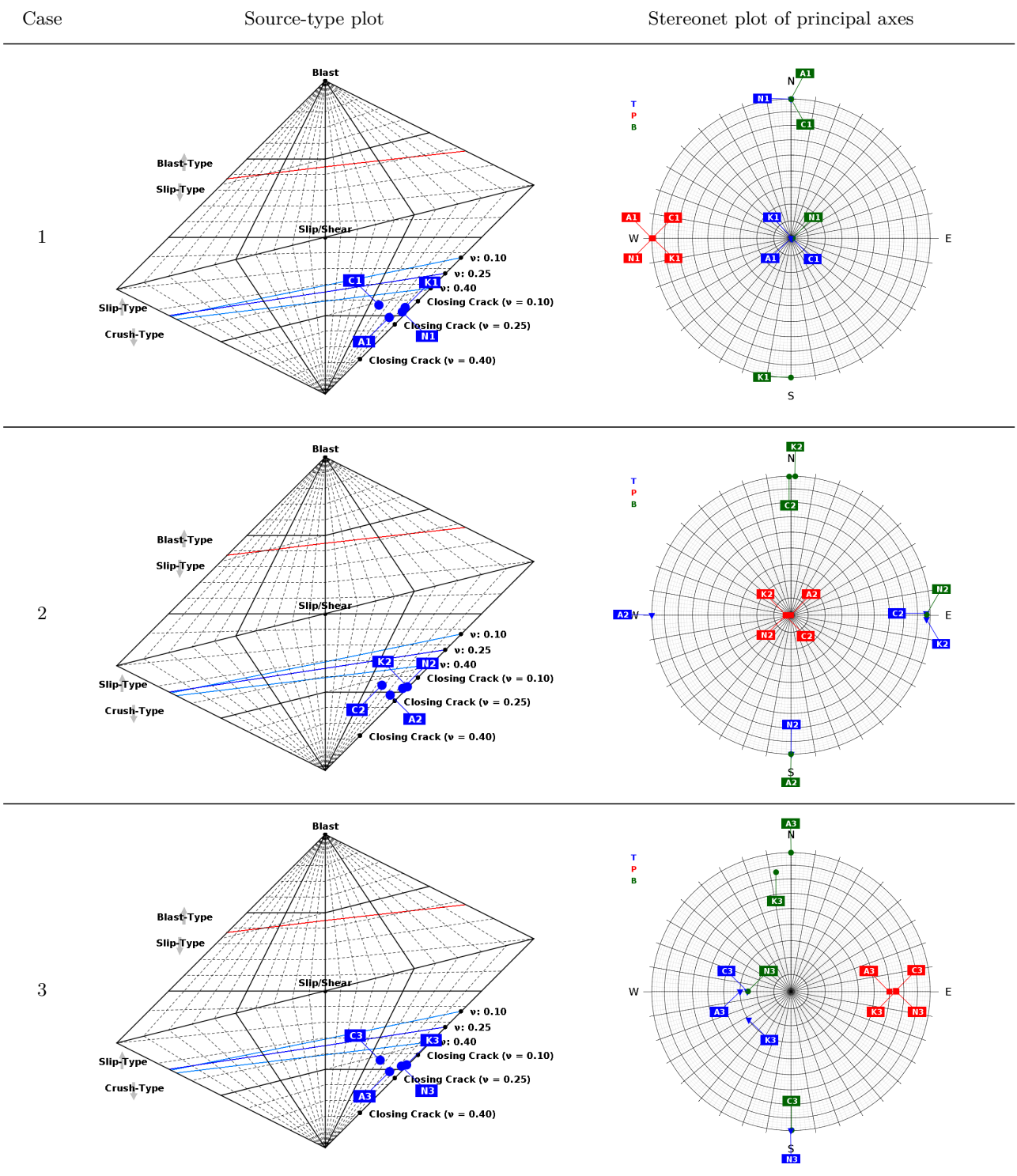




Table 2: continued.

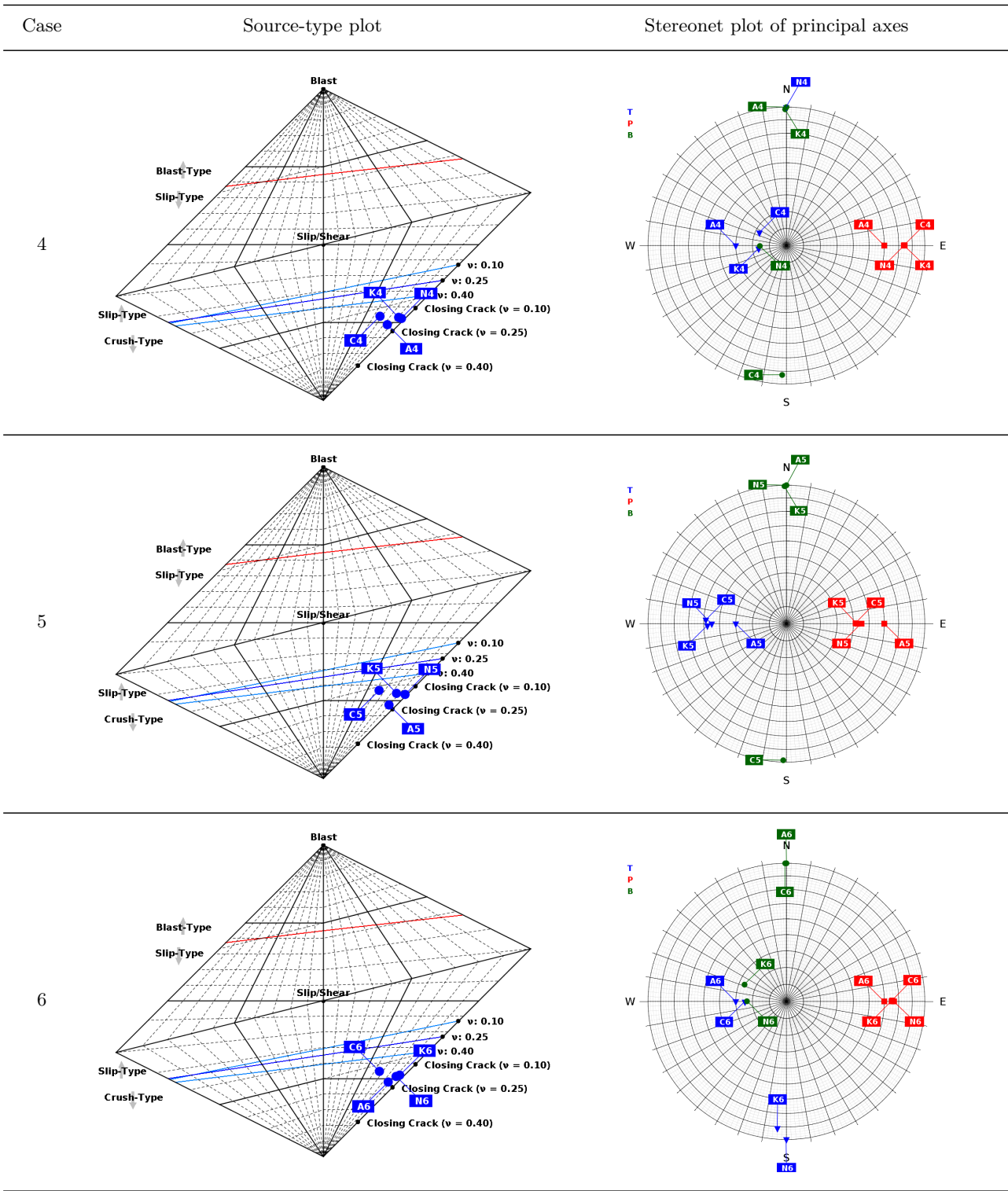


Table 1 also shows the contribution of the constituent terms of Equations (1) and (2) to the total solutions. For the Kirchhoff-type expression, it can be seen that  $|\mathbf{M}^T| < |\mathbf{M}^U| < |\mathbf{M}|$  in all five cases, which is a result of each term contributing similar content to the overall seismic mechanism; in a sense,  $\mathbf{M}^T$  and  $\mathbf{M}^U$  combine constructively to form  $\mathbf{M}$ . We note that while  $\mathbf{M} = \mathbf{M}^T + \mathbf{M}^U$  is independent of the contour selected from integration, the components are not; however, their constructive nature seems to hold in general (see Appendix A). Behavior is quite different for the adjusted conventional expression, where the terms  $\mathbf{M}^e$  and  $\mathbf{M}^u$  combine “destructively,” resulting in  $|\mathbf{M}| \lesssim |\mathbf{M}^e| < |\mathbf{M}^u|$  in each case: the closure of the tunnel (implosive  $\mathbf{M}^u$ ) needs to overcompensate for the dilation of the fracturing rockmass (explosive  $\mathbf{M}^e$ ). An important feature of the counteracting nature of  $\mathbf{M}^e$  and  $\mathbf{M}^u$  is the potential for a significant amount of inelastic deformation (large  $|\mathbf{M}^e|$ ) producing considerable excavation closure (large  $|\mathbf{M}^u|$ ) but resulting in relatively weak seismic radiation (small  $|\mathbf{M}|$ ). Physically, this means that large sudden inelastic deformation may constitute a small-magnitude seismic source if the deformed volume has poor mechanical coupling with the surrounding rock mass.

The conventional expression for a moment tensor {see, for example, Equation (3.32) in [1]} includes only the strain term  $\mathbf{M}^e$  of Equation (2). Such a definition suggests interpreting scalar moment in terms of average plastic strain; that is,  $|\mathbf{M}| \approx kV\overline{\Delta\epsilon^p}$ , where  $k$  is the relevant elastic moduli (shear modulus  $\mu$  is typically used) and  $V$  is the volume of inelastic deformation. However, the results presented here (in particular that  $|\mathbf{M}| \lesssim |\mathbf{M}^e|$ ) mean that this approach potentially leads to an underestimation of average plastic strain for events associated with dynamic stress fracturing around tunnels. It is more appropriate to interpret the scalar moment in terms of mechanical and geometric parameters describing fracturing around the tunnel. Such expressions will be presented in the next section.

### 3 Approximate description of sources

The numerical modelling of seismic source mechanisms presented in Section 2 is a useful instrument in the forensic analysis of strainbursts or seismic events accompanied by significant deformation of tunnels. However, building and solving such models may be computationally prohibitive. Furthermore, several iterations of building and solving would likely be required to produce a theoretical source mechanism that matches observations (including scalar moment). The situation would be complicated further in the case of the observation of multiple seismic events with the characteristic source mechanism features presented in the previous section (implosive isotropic component and pancake-shape CLVD component). To address these complications, this section discusses an approximate model for the source mechanism of such events that relies only on geometric and mechanical inputs, which provides a means for analysis without the use of numerical modelling.

#### 3.1 Effective cavity expansion

A tunnel and its associated damaged zone can be approximated by a stress-free elliptical cavity in an elastic medium. An example of such an approximation is shown in Figure 5 for the conceptual model discussed in Subsection 2.1. An appropriate cavity should, when loaded in the same manner as the tunnel itself, reproduce the major characteristics of stress and strain outside the tunnel’s damaged zone. Obviously, such a cavity cannot replicate all details of the actual stress and strain fields; for example, some parts of the damaged zone or even the interior of the tunnel can be located outside the cavity as shown in Figure 5, so modelled stress and strain in these areas will not be accurate. However, we shall show that such small-scale imperfections do not prohibit the selection of cavities that yield reasonable approximations of the seismic source mechanisms described by Equation (1).

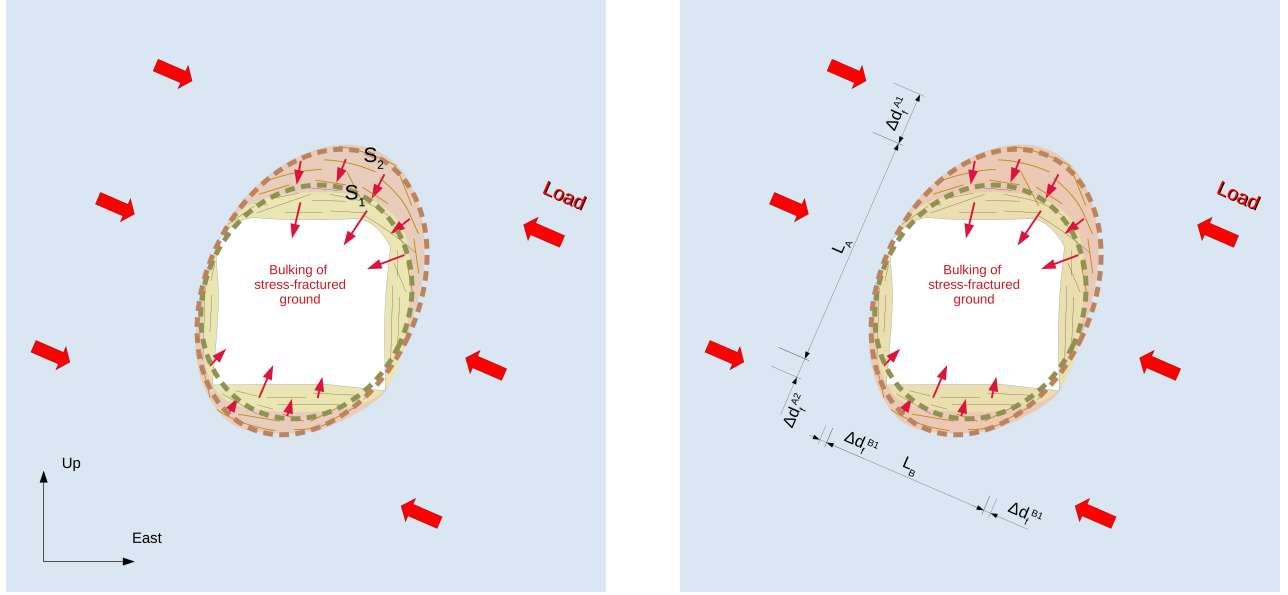


Figure 5: Approximation of a tunnel and its damage zone by an elliptical cavity (*left*). Geometrical parameters describing the model (*right*).

The discussed problem of stress fracturing around tunnels requires two elliptical cavities: one for the initial state prior to the expansion of the damaged region (the yellow zone in Figure 5) and another for the state after this expansion (the red region in Figure 5). Analytical expressions for stress and displacement around a two-dimensional elliptical cavity are presented in [20] for plane stress and plane strain (the latter being used here) and can be utilized in the Kirchhoff-type moment tensor definition of Equation (1) by selecting any contour  $S$  that encloses both ellipses. Note that we constrain the north-south extent of the surface  $S$  in the same manner as described in Subsection 2.2; that is, we effectively take a  $L_3 = 5$  m slice of the plane strain solution, which implies infinite extent of damage along the tunnel’s axis.

### 3.2 Numerical approximation

For the six cases considered in Section 2, we select approximating ellipses based on the depth of failure. In practice, the depth of failure can be evaluated through visual observation in boreholes or through the use of empirical relations to the magnitudes of principal stresses and the uniaxial compressive strength of the rockmass [5, 18]. We follow [26] in taking the depth of failure to be defined by the boundary between the inner and outer excavation damage zones, which is identified by the transition of tensile to compressive volumetric strain in the failed region. These tensile and compressive zones are shown in yellow/orange and blue, respectively, in Figure 6 for Case 3. The area defined by the tunnel’s profile and the tensile failed region is used to determine an ellipse based on moments of inertia [14]. In particular, the center of the ellipse coincides with the area’s center of mass, the orientation is taken to be the angle minimizing the area’s moment of inertia, and the major and minor semi-axes are selected such that the area and the ellipse have the same second moments of inertia. The ellipses derived for Case 3 are overlaid in Figure 6 along with displacement and traction computed on the same contour used in Section 2.3, which are adopted in Equation 1 to determine the mechanism shown.

Plots summarizing the elliptical approximation of the expansion of the damaged region are given in Appendix A and results of the corresponding seismic moment calculations are summarized in Tables 1 and 2 (listed as  $N$ ). Comparison with the respective Kirchhoff-type solutions of Subsection 2.3 indicates that the suggested approximation as the expansion of an elliptical cavity is reasonable:

- The seismic moment ratios range from 1.20 (Case 3) to 1.41 (Case 5), which corresponds to Hanks-Kanamori moment magnitude differences of 0.05 and 0.10, respectively. This slight overestimation

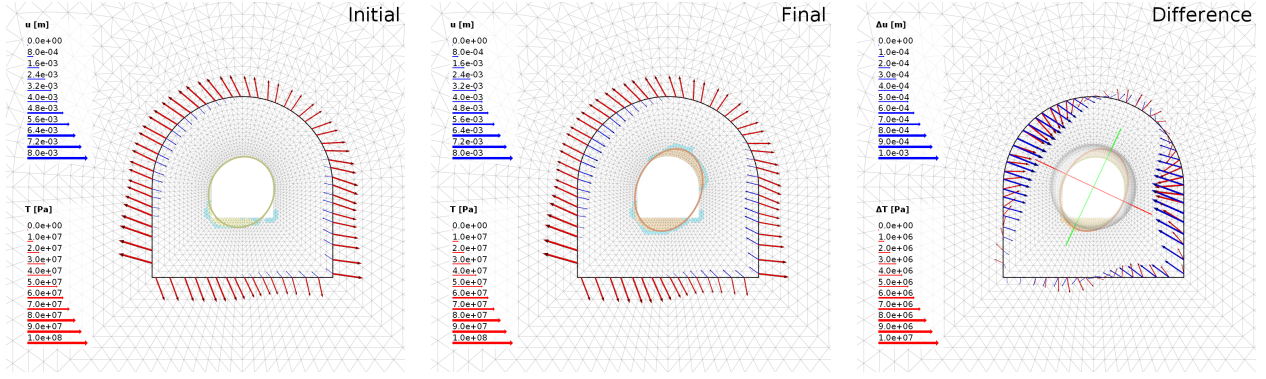


Figure 6: Illustration of the seismic mechanism calculation for Case 3 using fitted ellipses and Equation (1). Descriptions are provided in the text.

is possibly a result of the approach taken to selecting approximating ellipses.

- In most case, the source types for the suggested approximations deviate less from the Kirchhoff-type solution ( $K$ ), than the adjusted conventional solution ( $C$ ) does. The difference does not exceed 0.03 and 0.11 for the  $k$  (strength of the isotropic component) and  $T$  (deviation of the deviatoric component from a double-couple model) parameters, respectively.
- The maximum difference in the orientation of the P-axis from the Kirchhoff-type solutions does not exceed  $2.8^\circ$ . There is much larger variation in B- and T-axis orientation; however, this is to be expected given the previously discussed near degeneracy of the corresponding eigenvalues.

These deviations from the Kirchhoff-type solution are all within the typical uncertainty of source mechanisms evaluated from real data.

### 3.3 Analytical approximation

The results presented in Subsection 3.2 demonstrate that instances of dynamic stress fracturing around tunnels can be modelled as the expansion of an elliptical cavity. However, the ellipses used were derived from the results of numerical modelling of stresses and strains, and the calculation of the corresponding source mechanisms required numerical integration. In this subsection, we present a parameterization of the elliptical cavity expansion and a corresponding analytical expression for approximating the source mechanism.

Dynamic stress fracturing around a tunnel can be represented as a sudden increase  $\Delta d_f$  in the depth of failure. As shown in Figure 5, the original and expanded elliptical cavities can be parameterized in terms of this increase:

- We assume that the original and expanded cavities have minor axes aligned with the direction of loading. This is consistent with stress being concentrated in the tunnel sides orthogonal to loading, which facilitates growth of the damaged zone.
- The lengths of the major and minor axes of the initial ellipse are denoted as  $L_A$  and  $L_B$ , respectively. These represent the effective dimensions of the tunnel including its pre-existing damaged zone.
- The lengths of the post-expansion axes are  $L_A + \Delta d_f^A$  and  $L_B + \Delta d_f^B$ , where  $\Delta d_f^A = \Delta d_f^{A1} + \Delta d_f^{A2}$  and  $\Delta d_f^B = \Delta d_f^{B1} + \Delta d_f^{B2}$  are the increases in depth of failure in the directions of the major and minor axes, respectively.
- The extension of both the pre- and post-expansion cavities along the tunnel's axis is  $L_3$ .

In terms of the parameterization outlined above, it is possible to derive an approximate analytical expression for the source mechanism resulting from an elliptical cavity expansion. This is detailed in Appendix B, with the resulting expression being

$$M_{ij} = \begin{cases} C_M [\frac{\pi}{2}\nu + (1-\nu)C_1 - C_2] & \text{if } i, j = 1, \\ C_M [\frac{\pi}{2}(1-\nu) + \nu C_1 + C_2] & \text{if } i, j = 2, \\ C_M [\frac{\pi}{2}\nu + \nu C_1] & \text{if } i, j = 3, \\ 0 & \text{otherwise,} \end{cases} \quad (3)$$

where

$$\begin{aligned} C_M &= 2 \frac{1-\nu}{1-2\nu} \sigma_{\max} L_3 \overline{L_A} \Delta d_f^A, \\ C_1 &= \frac{\pi}{2} \frac{1}{k_\sigma} \frac{\Delta d_f^B}{\Delta d_f^A} \frac{\overline{L_B}}{\overline{L_A}}, \\ C_2 &= \frac{\pi}{8} (1-2\nu) (1 - \frac{1}{k_\sigma}) (\frac{\overline{L_B}}{\overline{L_A}} + \frac{\Delta d_f^B}{\Delta d_f^A}), \end{aligned}$$

$\overline{L_A} = L_A + \Delta d_f^A/2$  and  $\overline{L_B} = L_B + \Delta d_f^B/2$  are the mean of pre- and post-event effective tunnel dimensions,  $\sigma_{\max}$  and  $\sigma_{\min}$  are the maximum and minimum principal stresses orthogonal to the tunnel's axis,  $\nu$  is Poisson's ratio for the rockmass, and  $k_\sigma = \sigma_{\max}/\sigma_{\min}$ . Note that this expression is in a coordinate system defined by the tunnel and its loading, with  $\hat{x}_1$  in the direction of  $\sigma_{\min}$ ,  $\hat{x}_2$  in the direction of  $\sigma_{\max}$ , and  $\hat{x}_3$  directed along the tunnel's axis.

To verify the analytical approximations of Equation (3), we have parameterized the ellipses fitted in Subsection 3.2 in terms of  $L_A$ ,  $L_B$ ,  $\Delta d_f^A$ , and  $\Delta d_f^B$  as listed in Table 3. The remaining input parameters have been given in Section 2.2. The approximate seismic moments calculated using Equation (3) are summarized in Tables 1 and 2. There is a similar degree of agreement with the Kirchhoff-type solutions of Subsection 2.3 to that observed for the cavity expansion solutions relying on numerical integration presented in Subsection 3.2:

- The seismic moment ratios range from 1.21 (Case 2) to 1.40 (Case 4), which corresponds to Hanks-Kanamori moment magnitude differences of 0.05 and 0.10, respectively.
- In most cases, the source types for the suggested approximations do not deviate significantly further for the Kirchhoff-type solution ( $K$ ) than the numerical solutions ( $N$ ) do.
- The principal axes for the analytical solutions are fixed by the loading and tunnel orientation. The maximum difference in the orientation of the P- axis from the Kirchhoff-type solutions does not exceed 18°.

Again, these deviations from the Kirchhoff-type solution are all within the typical uncertainty of source mechanisms evaluated from real data.

Table 3: Geometric parameters of effective elliptical cavities fitted in Subsection 3.2.

Parameter	Case 1	Case 2	Case 3	Case 4	Case 5	Case 6
$L_A$ [m]	5.54	6.10	5.85	7.19	6.65	5.85
$L_B$ [m]	5.34	5.41	5.21	5.40	5.17	5.21
$\Delta d_f^A$ [m]	2.08	1.53	1.07	0.39	0.36	1.08
$\Delta d_f^B$ [m]	-0.16	0.02	-0.05	-0.03	0.05	0.03



The scalar seismic moment  $|\mathbf{M}| = \sqrt{(M_{11}^2 + M_{22}^2 + M_{33}^2)/2}$  for the expression of Equation (3) depends on  $C_M$ , ratios of geometric parameters ( $\overline{L_B}/\overline{L_A}$  and  $\Delta d_f^B/\Delta d_f^A$ ), the ratio of principal stresses orthogonal to the tunnel's axis ( $k_\sigma$ ), and the material's elastic properties ( $\nu$ ). However, it can be seen in Table 1 that  $|\mathbf{M}| \approx |C_M|$  across all six cases. To show that this agreement holds across a wide range of reasonable inputs, we consider variants on a “reference” mechanism with  $\overline{L_B}/\overline{L_A} = 0.8$ ,  $\Delta d_f^B/\Delta d_f^A = 0$ ,  $k_\sigma = 2$ , and  $\nu = 0.25$ . As is shown in the left of Figure 7, individually varying any of these four parameters over a wide range has little effect on the ratio  $|C_M|/|\mathbf{M}|$  or difference in moment magnitude  $\Delta m_{\text{HK}}$ . These ranges and the corresponding bounds on  $|C_M|/|\mathbf{M}|$  and  $\Delta m_{\text{HK}}$  are listed in Table 4. The effect of varying multiple parameters has also been investigated by uniformly sampling  $\overline{L_B}/\overline{L_A}$ ,  $\Delta d_f^B/\Delta d_f^A$ ,  $\log_{10} k_\sigma$ , and  $\nu$  uniformly over the same ranges to produce the histogram on the right of Figure 7. As listed in Table 4, this still results in relatively stable values of  $0.55 < |C_M|/|\mathbf{M}| < 1.10$  and  $-0.17 < \Delta m_{\text{HK}} < 0.03$ . As such,

$$|\mathbf{M}| \approx 2 \frac{1 - \nu}{1 - 2\nu} |\sigma_{\text{max}}| L_3 \overline{L_A} \Delta d_f^A \quad (4)$$

can be used as a simple yet quite accurate approximation to the scalar moment that can be derived from the full moment tensor solution of Equation (3). In the case of  $\nu \approx 0.25$ , this reduces to the even simpler  $|\mathbf{M}| \approx 3 |\sigma_{\text{max}}| L_3 \overline{L_A} \Delta d_f^A$ .

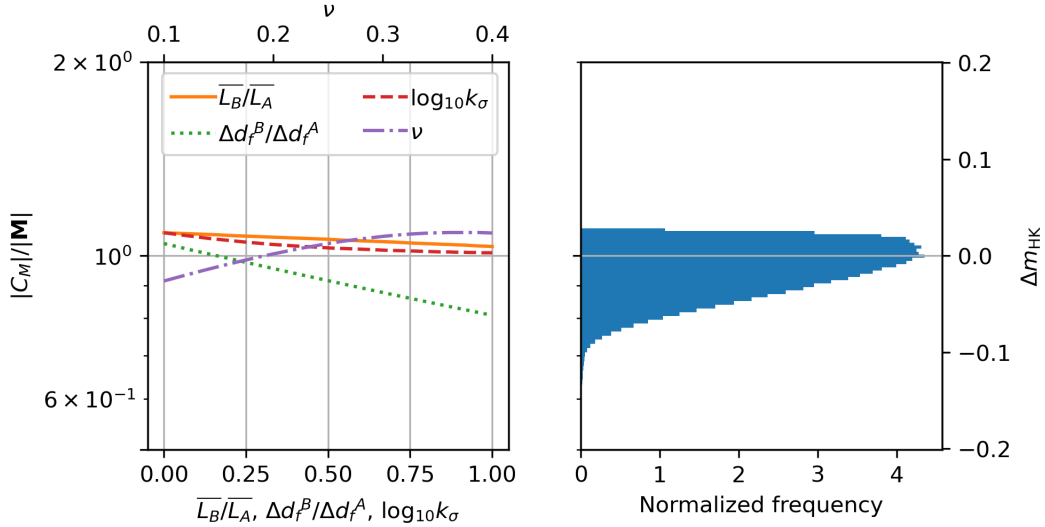


Figure 7: Approximation of scalar moment  $|\mathbf{M}|$  for the mechanism described in (3) by the parameter  $C_M$ . The effect of varying one of  $\overline{L_B}/\overline{L_A}$ ,  $\Delta d_f^B/\Delta d_f^A$ ,  $k_\sigma$ , or  $\nu$  with respect to the reference mechanism ( $\overline{L_B}/\overline{L_A} = 0.8$ ,  $\Delta d_f^B/\Delta d_f^A = 0$ ,  $k_\sigma = 2$ , and  $\nu = 0.25$ ) on the ratio  $|C_M|/|\mathbf{M}|$  (left). Histogram of  $|C_M|/|\mathbf{M}|$  values resulting from sampling  $\overline{L_B}/\overline{L_A}$ ,  $\Delta d_f^B/\Delta d_f^A$ ,  $\log_{10} k_\sigma$ , and  $\nu$  uniformly over the same ranges (right). The right vertical axis shows the difference between  $|\mathbf{M}|$  and  $|C_M|$  expressed in terms of Hanks-Kanamori moment magnitude.

Table 4: Maximum/minimum ratios  $|C_M|/|\mathbf{M}|$  and moment magnitude differences  $\Delta m_{\text{HK}}$  for mechanisms varying from the reference case ( $\overline{L_B}/\overline{L_A} = 0.8$ ,  $\Delta d_f^B/\Delta d_f^A = 0$ ,  $k_\sigma = 2$ , and  $\nu = 0.25$ ) by the listed parameter(s).

Parameter varied	$\overline{L_B}/\overline{L_A}$	$\Delta d_f^B/\Delta d_f^A$	$k_\sigma$	$\nu$	All
Parameter minimum	0	0	1	0.15	-
Parameter maximum	1	1	10	0.4	-
Minimum $ C_M / \mathbf{M} $	1.03	0.81	1.01	0.91	0.55
Maximum $ C_M / \mathbf{M} $	1.08	1.05	1.09	1.09	1.10
Minimum $\Delta m_{\text{HK}}$	0.01	-0.06	0.00	-0.03	-0.17
Maximum $\Delta m_{\text{HK}}$	0.02	0.01	0.02	0.02	0.03

### 3.4 Depth of failure inversion

Rearranging Equation (4) yields

$$\Delta d_f^A = \sqrt{L_A^2 + \frac{1-2\nu}{1-\nu} \frac{|\mathbf{M}|}{|\sigma_{\max}|L_3}} - L_A. \quad (5)$$

In practice, this equation can be used to infer the depth of failure increase  $\Delta d_f^A$  from the observed seismic moment  $|\mathbf{M}|$  assuming knowledge (or reasonable estimates) of  $L_A$ ,  $\nu$ ,  $|\sigma_{\max}|$ , and  $L_3$ . As a demonstration of this process and to give an idea of the uncertainties involved, we have done this for the six modelled cases considered. In each case, we take  $|\mathbf{M}|$  as listed in the Kirchhoff column of Table 1 with an uncertainty of  $\pm 40\%$  (corresponding to roughly  $\pm 0.1 m_{\text{HK}}$ ),  $L_A = 6 \text{ m} \pm 20\%$ ,  $\nu = 0.25 \pm 10\%$ ,  $L_3 = 5 \text{ m} \pm 20\%$ , and  $|\sigma_{\max}| = k|\sigma_{\min}| \pm 10\%$ . The inferred values obtained from Equation 5 are listed in Table 5. For comparison, “measured” depth of failure increases are also listed in Table 5, which have been determined based on the depth of failure definition discussed in Section 3.2. In particular, the depth of failure increase has been averaged within a  $45^\circ$  window centered at the direction of minor loading (that is,  $22.5^\circ$  either side). This procedure has been chosen eliminate any impact from the method of selecting approximating ellipses and to more closely match the methodology of depth of failure measurement using boreholes (we note, however, that the values do not vary significantly from those derived from approximating ellipses as listed in Table 4). In general, it can be seen that the inferred and measured values are in reasonable agreement given their respective uncertainties.

Table 5: Inferred and measured depth of failure increases for the six cases modelled.

Case	$\Delta d_f^A$ inferred [m]	$\Delta d_f^A$ measured [m]
1	$1.43 \pm 0.64$	$1.95 \pm 0.24$
2	$1.26 \pm 0.57$	$1.65 \pm 0.07$
3	$0.81 \pm 0.38$	$0.93 \pm 0.29$
4	$0.32 \pm 0.15$	$0.31 \pm 0.13$
5	$0.30 \pm 0.15$	$0.32 \pm 0.22$
6	$0.79 \pm 0.37$	$0.91 \pm 0.30$

## 4 Examples of Seismic Events from a Mine

In this section, the source model presented in Subsection 3.3 is applied to real data, which comes from a seismic monitoring system operating in a deep underground hard-rock mine in Western Australia. This system is composed of geophones with natural frequencies of 4.5 Hz and 14 Hz that are installed

and grouted in boreholes away from excavations. The acquired seismic data is of high quality: many waveforms are recorded by sites within line-of-sight of the source (that is, not shielded by excavations) and consist of P- and S-wave pulses with little coda. As a result, the use of an elastodynamic Green’s function  $\mathbf{G}$  for homogeneous isotropic space is appropriate. Given the system’s good coverage of sources and the simplicity of the recorded waveforms, source mechanisms of events can be analyzed in detail.

## 4.1 Overview

A significant seismic event ( $m_{\text{HK}} = 2.3$ ) was recorded in the deep levels of the mine on 8 June 2019. The event was followed by a strong aftershock sequence, which included  $m_{\text{HK}} = 2.0$  and  $m_{\text{HK}} = 1.7$  events within three minutes of the mainshock and a  $m_{\text{HK}} = 1.9$  event approximately 27 hours later. There was no direct spatial or temporal association of the mainshock with the excavation of large volumes of rock, with the largest nearby stope blasting occurring more than four days prior to the event.

After the aftershock activity decayed, the tunnels were inspected. Damage was observed at four levels, manifesting primarily in the form of floor heave, an example of which is shown in Figure 8. There were also isolated cases of support deformation and failure in the roof (back) of the tunnels (bottom of Figure 8) and shakedown of rocks from the lower unsupported parts of tunnels. This association of major damage with floor and backs is consistent with expectation given that maximum and intermediate (compressional) principal stresses are subhorizontal.

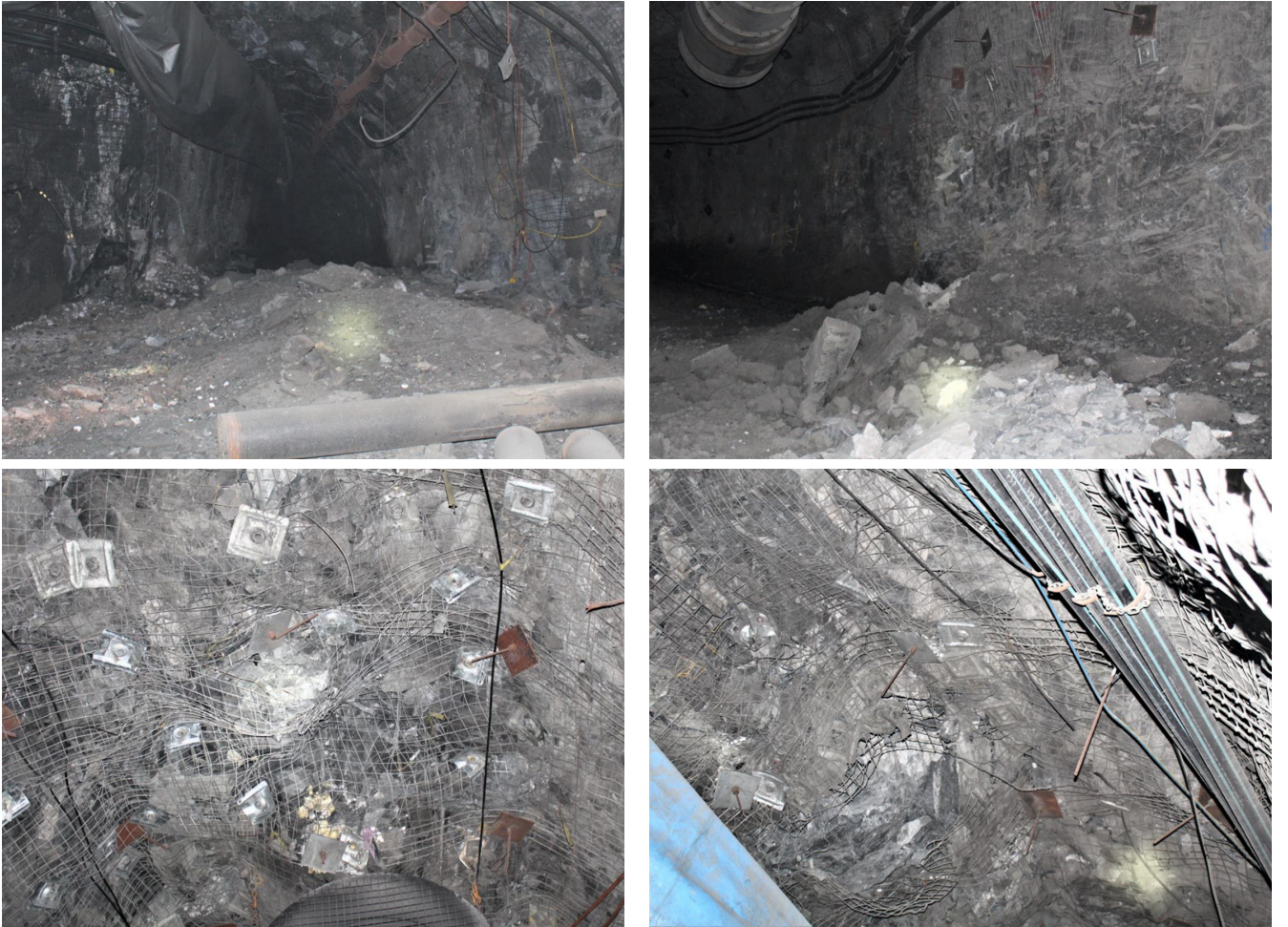


Figure 8: Damage observed underground: floor heave (*top*) and deformation of the supported roof (*bottom*).



Source mechanisms were calculated for 185 out of 220 events recorded within 48 hours of the mainshock (including all 19 events with  $m_{HK} > 0.0$ ). These mechanisms, with the mainshock excluded, are shown in Figure 9. The results of full-waveform inversion for one of these events is summarized in Figure 10, which demonstrates a good fit between observed and synthetic waveforms.

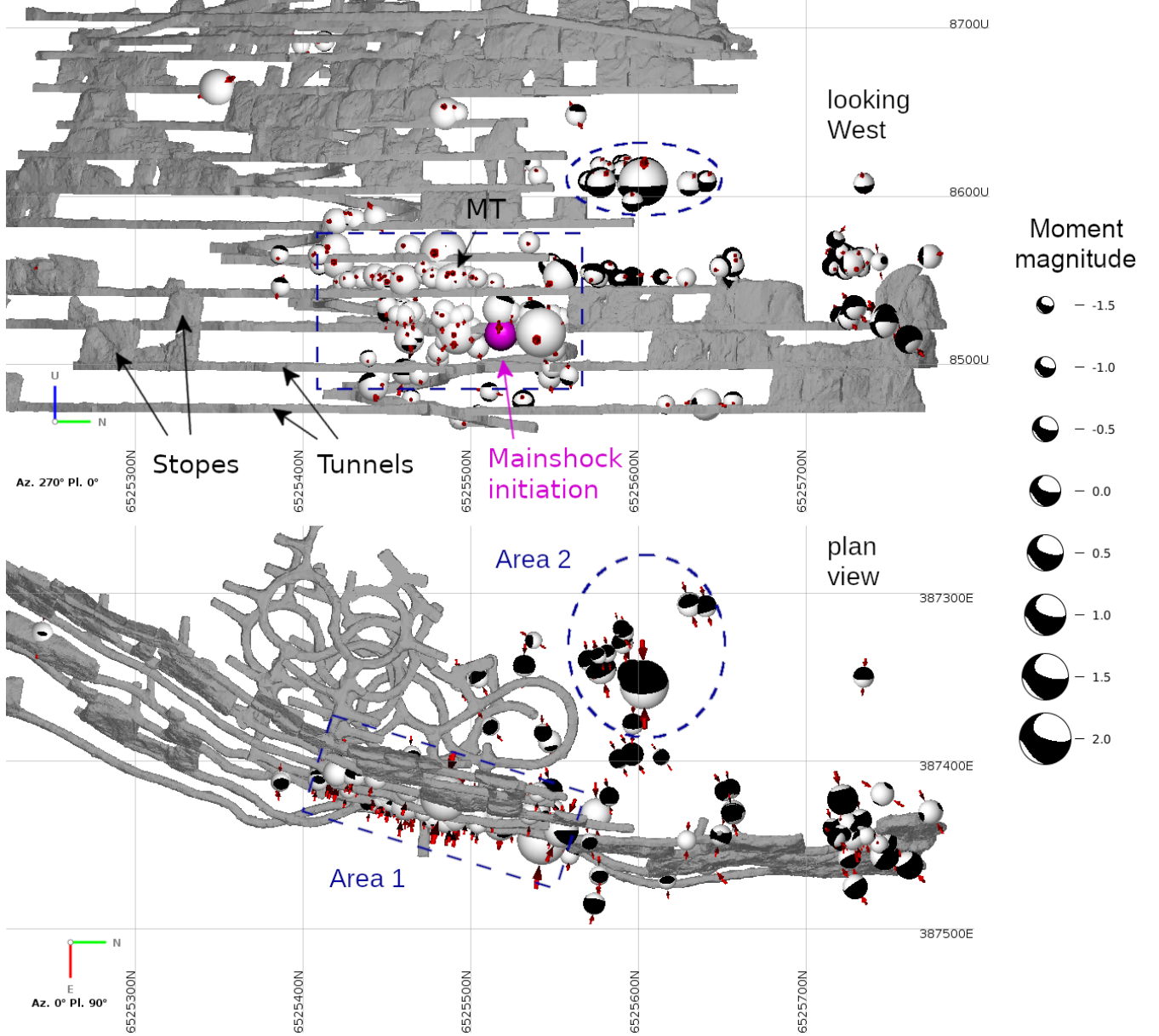


Figure 9: Analyzed seismicity presented in a form of beachballs sized according to  $m_{HK}$ . Red dipoles represent the P-axes of source mechanisms. The gray wireframes describe excavations (tunnels and stopes from which ore has been extracted) at the time of the analyzed seismic event. The two contoured areas (1 and 2) are described in the text. The mainshock is represented by a magenta sphere located at the inferred point of initiation (not sized by  $m_{HK}$ ).

Spatially, there are several groups of events in the dataset analyzed. Those defined by Areas 1 and 2 as contoured in Figure 9 are considered:

- The events in Area 1, which includes the mainshock, are clustered around tunnels (mainly ore drives), and the majority of them (80%) occurred within 24 hours of the mainshock. In total, 103

mechanisms were determined for events in this area, which includes the mainshock and previously mentioned  $m_{HK} = 2.0$  and  $m_{HK} = 1.7$  aftershocks. As shown in Figure 11, the majority of these mechanisms have a significant implosive component, a deviatoric component ranging from double couple to pancake-shaped CLVD, and a principal axis oriented approximately orthogonal to the direction of the ore drives. The locations and mechanisms of these events suggest interpretation in terms of the processes discussed in previous sections; that is, as episodes of dynamic stress fracturing around tunnels and the associated convergence of surrounding rockmass. In particular, the loading orientation and distribution of damage resemble Case 1 as considered in Sections 2 and 3 (and presented graphically in Appendix A).

- The events in Area 2 locate away from excavations in the footwall of the orebody and occurred more than 26 hours after the mainshock. Mechanisms were determined for 12 events in this area, including the  $m_{HK} = 1.9$  event, and all have a significant double-couple component as shown in Figure 11. The locations of these sources lie approximately on a common plane with a dip of  $15^\circ$  and dip direction of  $65^\circ$  (strike of  $335^\circ$ ), which is also consistent with the inferred nodal planes as shown in a stereonet in Figure 11. It follows that it is appropriate to interpret this cluster of events as episodes of slip (reverse faulting) along such a plane.

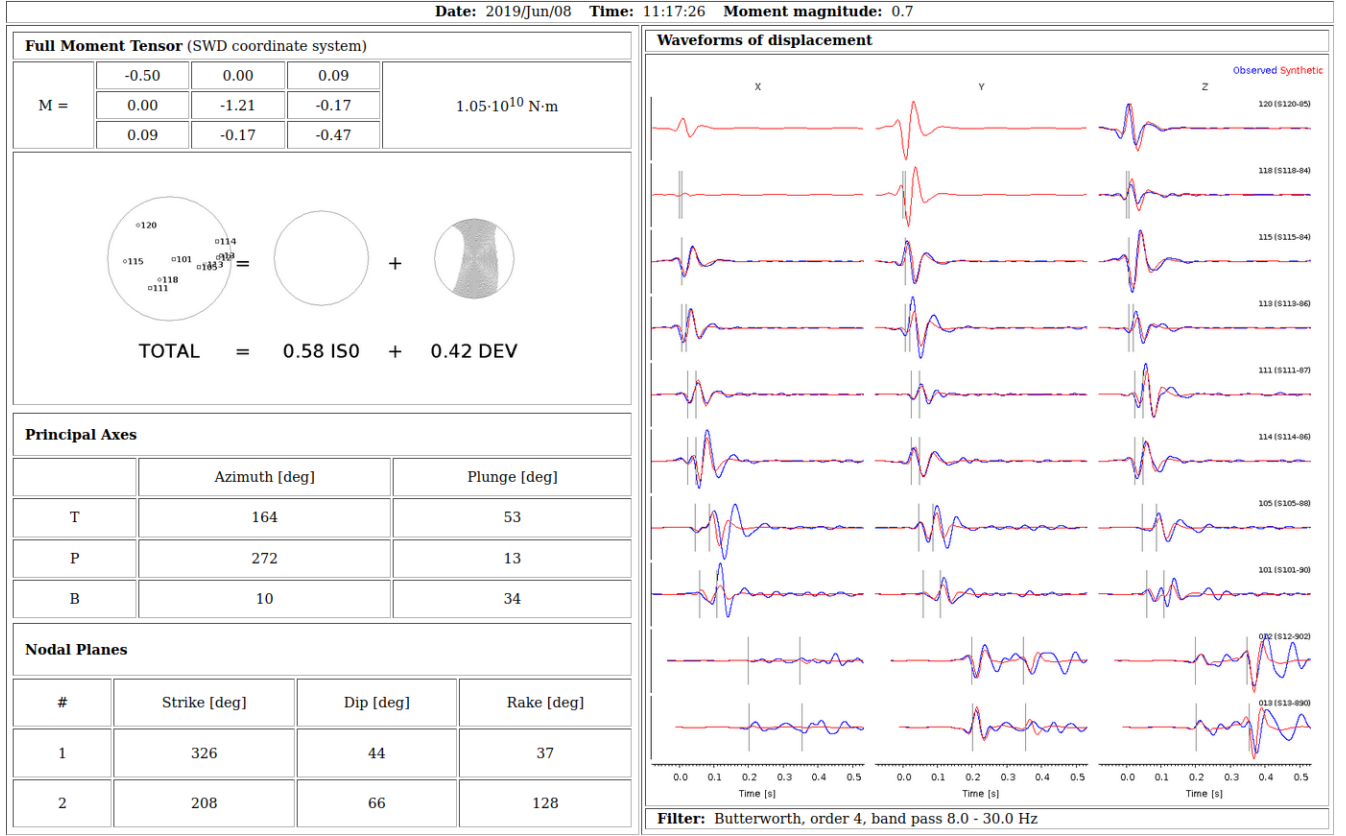
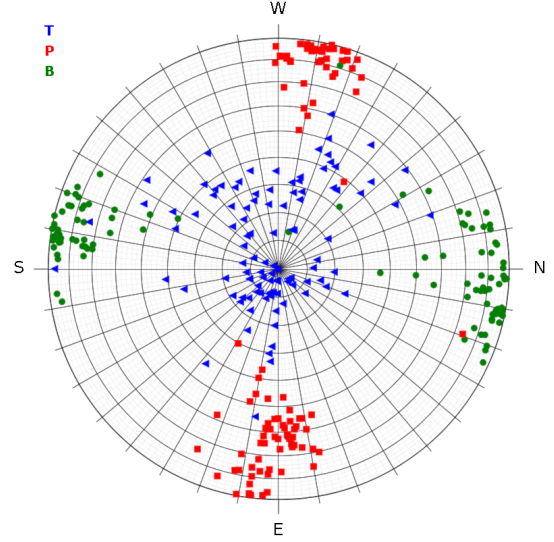
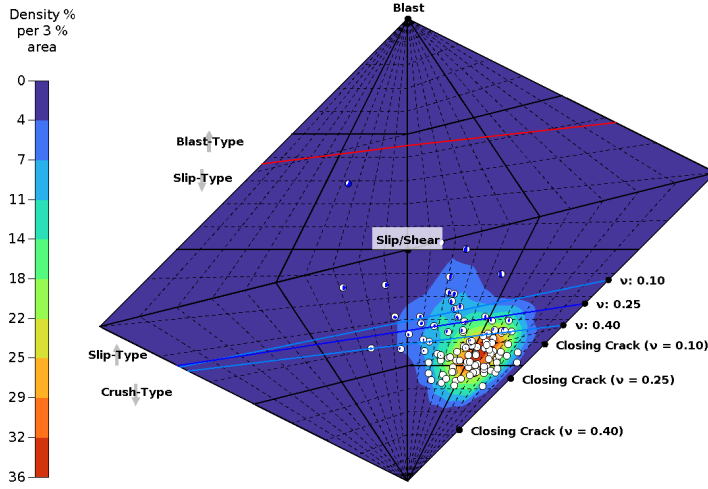


Figure 10: Results of moment tensor inversion for a medium-size seismic event marked as “MT” in Figure 9. Inverted source mechanism of the event (*left*). Observed waveforms of displacement are compared with the waveforms modelled for the inverted moment tensor (*right*). Sensor response is taken into account in the synthetic waveforms. A 4th-order Butterworth bandpass 8-30 Hz filter is applied to both observed and synthetic waveforms. Vertical gray lines mark the arrivals of direct P- and S-waves picked from unfiltered waveforms.



## Area 1



## Area 2

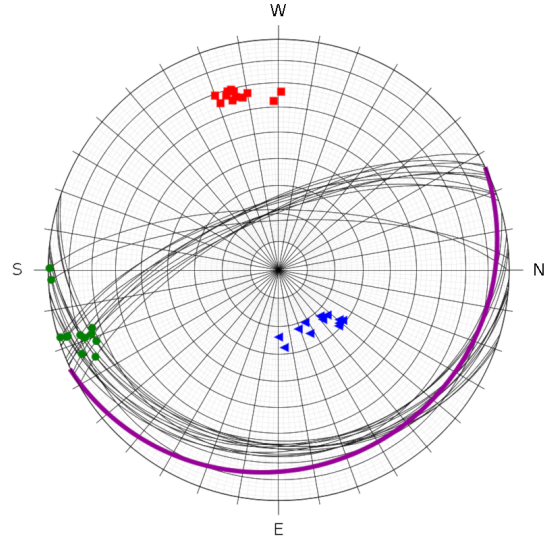
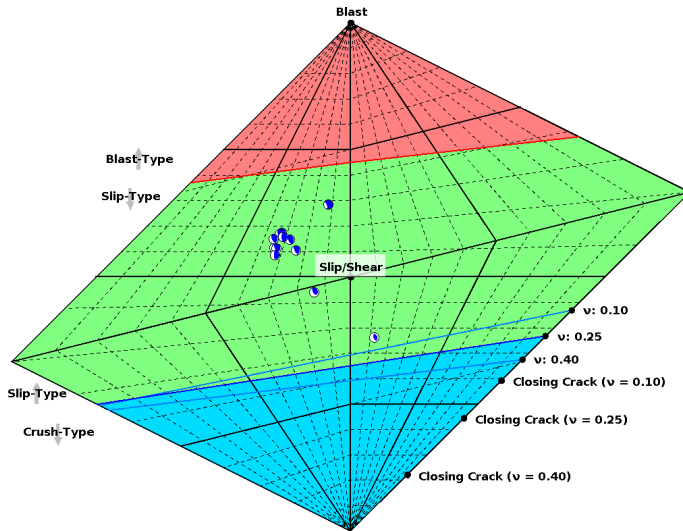


Figure 11: Characteristics of source mechanisms of events recorded in two areas contoured in Figure 9. Note that the stereonets are rotated  $90^\circ$  clockwise to match the view in Figure 9. The orientation of the common location plane of events in the Area 2 is shown in magenta in the associated stereonet.

## 4.2 Analysis of the mainshock

As shown in Figure 12, the mainshock waveforms are complex. This cannot be fully explained simply by the effects of wave propagation through an inhomogeneous medium as smaller events in the same area yield relatively simple waveforms, which are dominated by direct P- and S-waves. This indicates that the complexity results from the mainshock source consisting of multiple episodes of failure distributed in time (and likely space). Waveforms observed at distance sites (such as those with indices 12 and 13 in Figure 12) support this view, with at least three P-wave pulses visible: an initial wave, which was picked for location; a stronger one approximately 35 ms later; and one with even greater amplitude approximately 80 ms after the initial arrival. Although less clear, similar patterns can also be seen in the S-waves. At sites closer to the source (such as those with indices 113 and 114 in Figure 12), there is greater overlap of P- and S-waves, which makes identification of individual pulses more difficult.

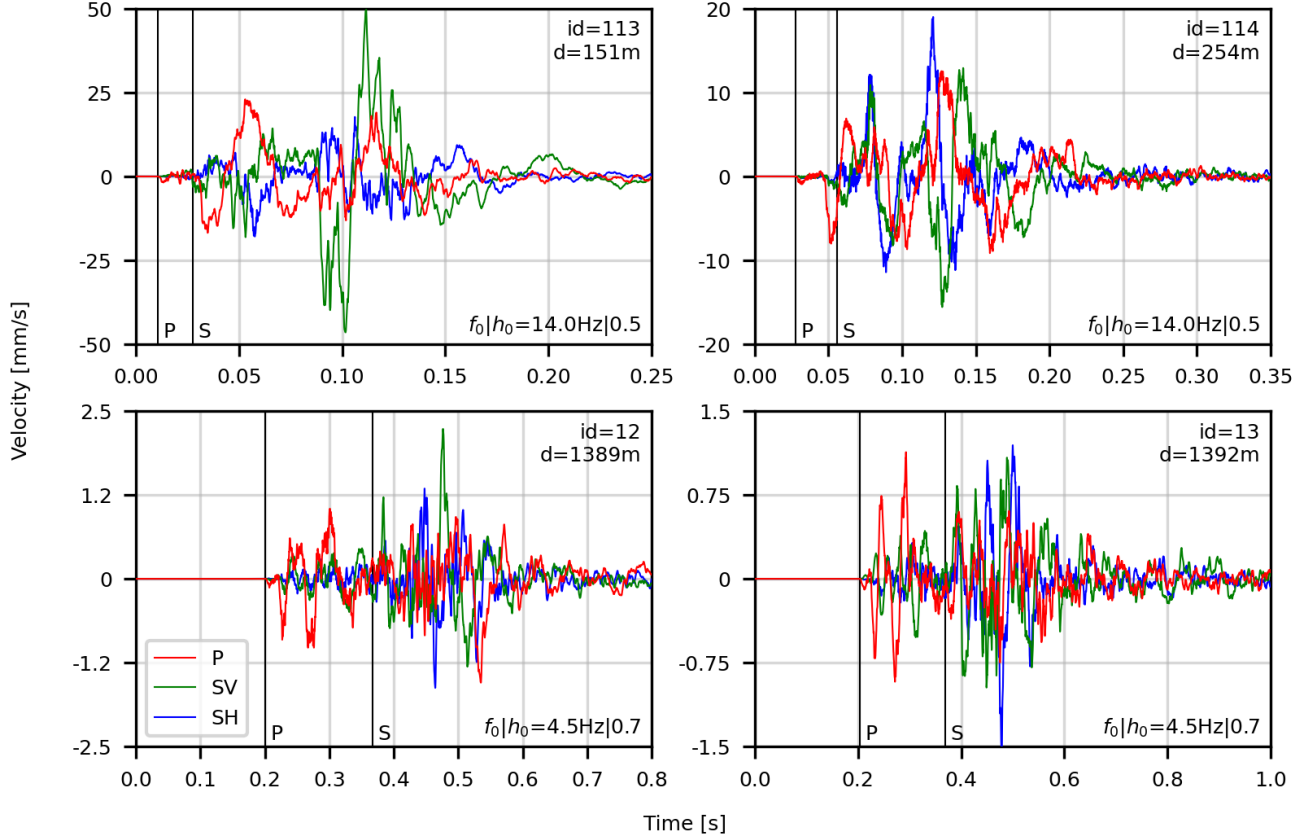


Figure 12: Examples of the mainshock waveforms as recorded at four representative sites: two located close to the source (*top*) and two far from the source (*bottom*). Each seismogram is rotated into a local P-SV-SH coordinate system of site, where the P-axis corresponds to the direction of strongest motion after the selected P-wave arrival (shown by a vertical line), while SV- and SH-axes are selected to be orthogonal to P-axis with the added constraint of the SH-axis being horizontal. Listed in the top right of each seismogram are site index (id) and distance  $d$  from the point of initiation. The natural frequency  $f_0$  and damping coefficient  $h_0$  of the geophones are listed in the bottom right.

Interpretation of the mainshock source and its relation to observed damage is not straightforward. In particular, interpretation in terms of slip along a plane is not supported by any clear planar structure in the immediate aftershocks in Area 1 (the inferred weak plane in Area 2 lies a significant distance from the mainshock’s point of initiation, and only became active 26 hours later; other clusters of aftershocks dominated by double-couple mechanisms are similarly distant in terms of space and time). As noted in Subsection 4.1, the mechanisms of aftershocks in Area 1 are consistent with dynamic stress fracturing around tunnels as discussed in Sections 2 and 3 (significant implosive and pancake-shaped CLVD components and a P-axis approximately orthogonal to the direction of the tunnels). This suggests the hypothesis that the mainshock source is composed of cascading stress fracturing around tunnels, in which damage around one section of tunnel rapidly transfers load to neighboring sections (either on the same or adjacent levels), resulting in expansion of the damaged region.

To test this hypothesis of cascading stress fracturing, we employ a variant of the procedure of [12] by constructing a distributed source model based on the locations of damage and immediate aftershocks, with parameters of the subsources being inverted from velocity waveforms and interpreted in terms of the model proposed in Section 3. The details of the distribution of 29 employed subsources is shown in Figure 13, each of which corresponds to a  $21 \times 21$  m square element normal to the expected orientation of the maximum principal stress orthogonal to the tunnel’s axis  $\sigma_{\max}$ . Also shown is the assumed time evolution

of the source: radial propagation from the point of initiation at an apparent velocity of  $750 \text{ ms}^{-1}$ .

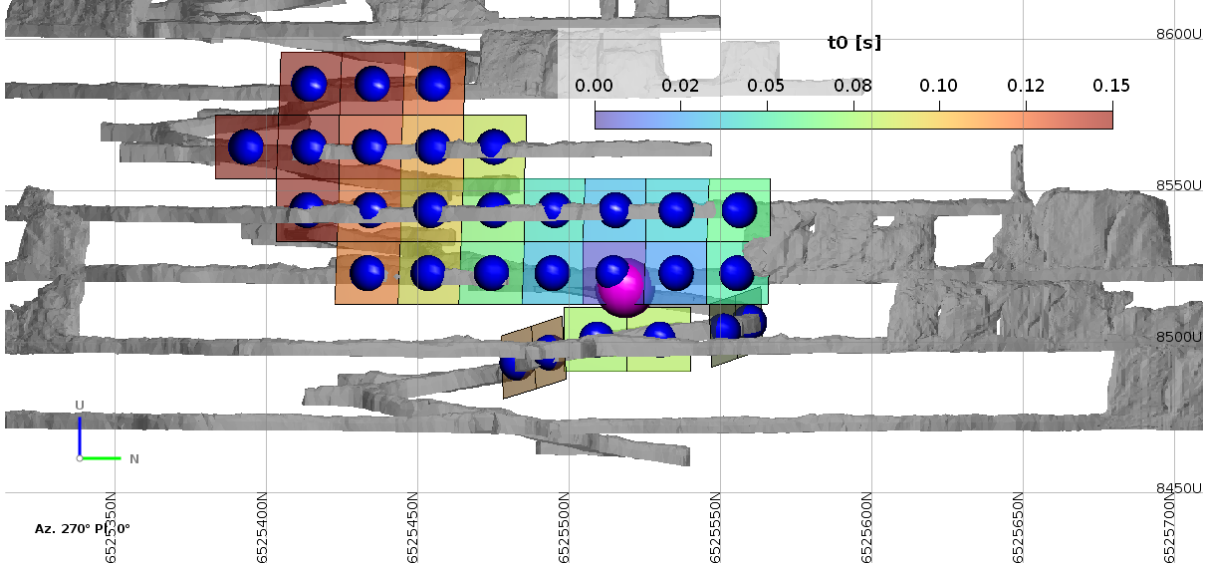


Figure 13: Parametrization of the mainshock finite source. Blue spheres describe 29 point sources distributed along the tunnels where damage and aftershocks were observed. Each of these sources describes the convergence and ride of a corresponding  $21 \times 21 \text{ m}$  element. These elements are colored by delay  $t_0$  relative to initiation, which occurred at the point marked by the magenta sphere.

Inversion of subsource parameters was performed using a variant of the slip inversion framework outlined in [24]. In the original framework, a pure double-couple subsource is assumed, with inversion being performed for slip in two mutually orthogonal directions in the plane of the corresponding square element. In our approach, we assume a subsource decomposition in terms of two different parameters. The first of these is the magnitude of a mechanism composed of three orthogonal compressional vector dipoles with an amplitude ratio of  $1 : 1 : (1/\nu - 1)$ , where the latter dipole is oriented orthogonal to the square element [this mechanism approximates the point-source model suggested in Equation (3)]. The second parameter is the amplitude of slip along the square element in a prescribed direction, which we take to be vertical (corresponding to reverse faulting). The technical aspects of inverting for the subsource parameters by matching observed and synthetic waveforms are summarized below.

- The elastodynamic Green’s function for homogeneous isotropic space was used.
- Matching was performed using velocity waveforms filtered below 100 Hz (as opposed to the displacement waveforms used in the point-source inversions discussed in Section 4.1).
- To permit variation around the prescribed radial evolution, the time history of each subsource was parameterized using the multi-time-window method of [24, 12]. In particular, 15 time steps of 2.5 ms centered around the prescribed time  $t_0$  were used, leading to  $870 = 29 \times 2 \times 15$  unknowns for which to invert (29 sources, two components, and 15 time steps).
- Nonnegative least square inversion was employed [24] to ensure that deformation at the source (convergence and slip) is unidirectional (that is, it does not change in sign).
- The total scalar seismic moment of all subsources was constrained by the low-frequency plateau of the source spectra ( $3.2 \times 10^{12} \text{ N} \cdot \text{m}$ , which corresponds to  $m_{\text{HK}} = 2.3$ ).

The observed and synthetic waveforms resulting from inversion are compared in Figure 14. A reasonable fit can be seen between the two, particularly in the initial and middle sections of the waveforms. There

is some discrepancy in the tail of waveforms at more distance sites; however, this may be related to imperfections introduced by the adopted Green's function, and so we have not attempted to reduce the misfit by increasing the model's complexity (that is, adding more subsources or extending their duration).

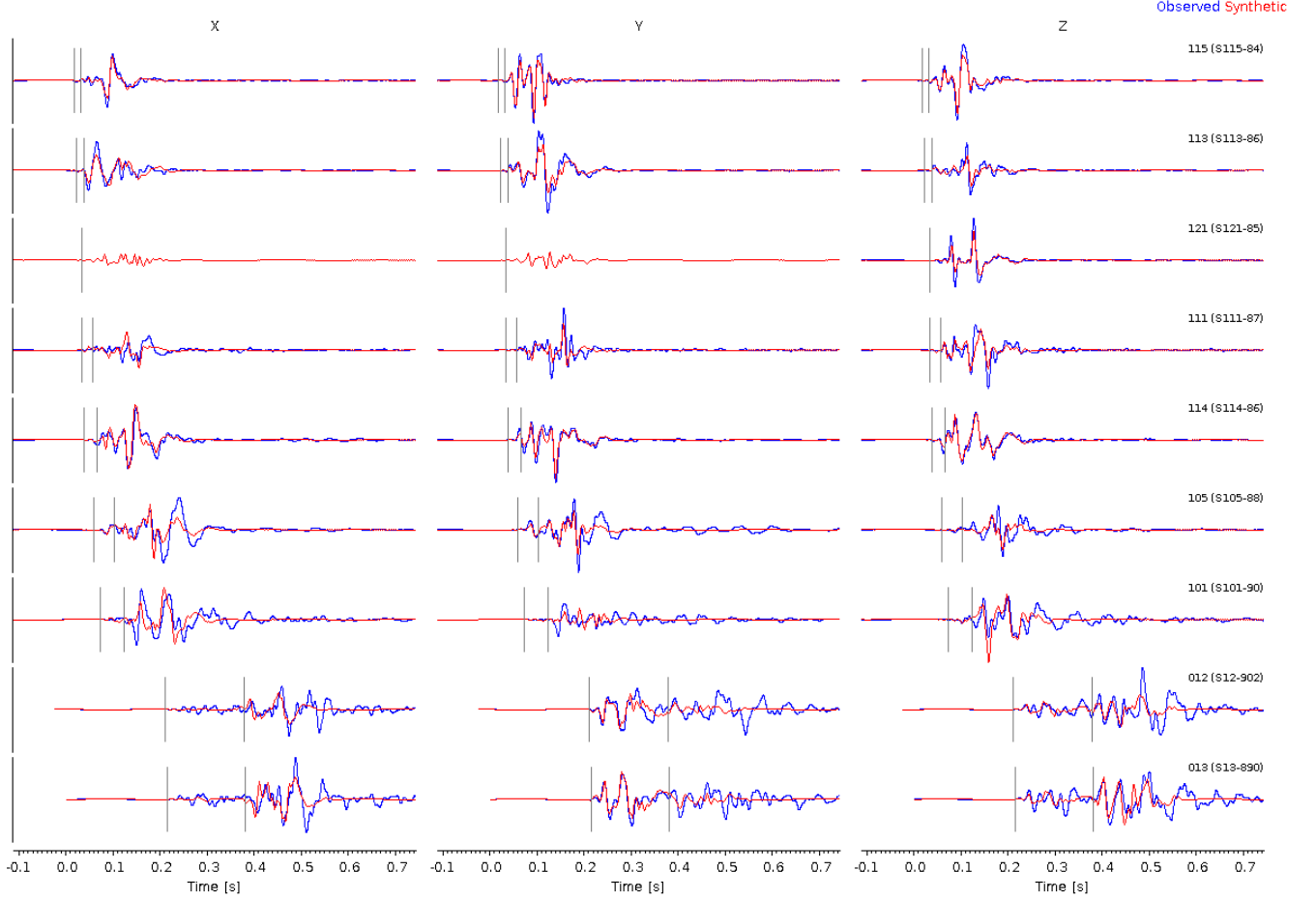


Figure 14: Fit of velocity waveforms obtained from finite-source inversion. Note that for each site, the waveforms have been normalized by maximum observed amplitude.

The left of Figure 15 shows the mechanisms of the subsources summed over the 15 time steps. The majority of these are dominated by implosive and pancake-shaped CLVD content, with double-couple content being less significant. As such, it is appropriate to interpret their scalar moments in terms of the model of Equation (4), which permits evaluation of a corresponding increase in the depth of failure  $\Delta d_f^A$  using Equation 5. Other required parameters have been selected as follows:

- Poisson's ratio of  $\nu = 0.23$  (inferred from seismic data).
- Maximum stress orthogonal to the tunnel's axis of  $\sigma_{\max} = -90$  MPa (based on elastic stress modelling results that take the *in situ* stress field and stress induced by stopes into account).
- Extent along the tunnel's axis of  $L_3 = 21$  m (according to the discretization of the finite source).
- Effective tunnel dimension of  $L_A = 7.0$  m (which incorporates the design tunnel height and presumed pre-event depth of failure of 1 m in both the roof and floor).

The obtained values of  $\Delta d_f^A$  are shown in the right of Figure 15 and have a maximum of 6.7 m, mean of 2.8 m, and median of 2.4 m. These values are not inconsistent with the observed damage, from which it follows that the suggested hypothesis of cascading stress fracturing around tunnels is plausible.

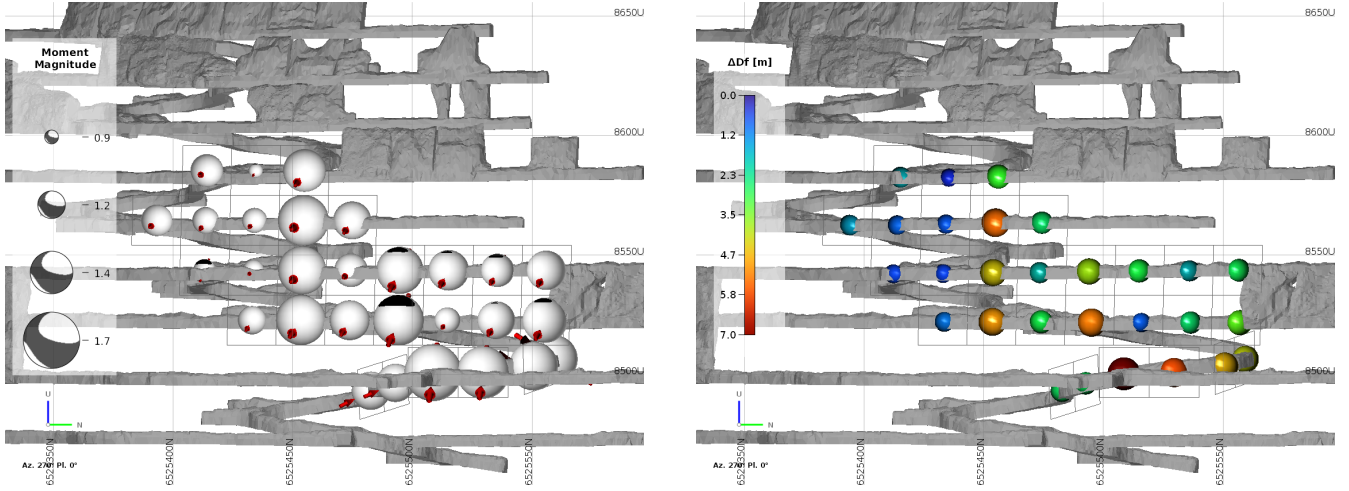


Figure 15: Results of inversion and interpretation of finite source parameters. The mechanisms of sub-sources are shown as beachballs sized according to  $m_{HK}$  and P-axes depicted by red dipoles (*left*). The evaluated increase in the depth of failure is shown by spheres colored by  $\Delta d_f^A$  and with diameter of  $L_A + \Delta d_f^A$  (*right*).

### 4.3 Analysis of smaller-scale seismicity

Figure 16 shows seismicity observed over a six-month period (1 January to 8 June 2019) prior to the large event considered in Subsection 4.2. In total, 1047 events were recorded, of which mechanisms were determined for 877 (including all events with  $m_{HK} > 0.0$ ). This seismicity can also be divided into several spatial groups, with those events in Area 3 (as contoured in Figure 16) being our focus here. As shown in Figure 16, these events have similar characteristics to the mainshock and its aftershocks in Area 1: clustering around the orebody in the proximity of the tunnels (ore drives), significant implosive and pancake-shape CLVD components, and P-axes approximately orthogonal to the direction of the drives. Again, these features suggest interpretation in terms of episodes of sudden stress fracturing in the roof and/or floor of the ore drives accompanied by horizontal elastic convergence of the surrounding rockmass.

Beyond this qualitative interpretation, an estimate of the increase in depth of failure can be made by mapping the source parameters of seismic events to the tunnels and determining  $\Delta d_f^A$  from scalar moment using Equation (5). The direction of this increase is controlled by the P-axis orientations of the projected mechanisms (we omit further details of this mapping process for the sake of brevity). The results of this procedure are presented in Figure 16, where it can be seen that the largest increase in depth of failure is expected to be in the roof and floor (due to the subhorizontal loading) of the tunnels in the central part of Area 3. In comparison to the values determined for the mainshock, these increases are relatively minor, not exceeding 0.35 m.

This example serves to demonstrate the possibility of quantitative monitoring of damage zone evolution around tunnels using seismic data. However, the suggested approach requires testing (including the comparison with borehole measurements), and this deserves a separate study. An important aspect of the employed mapping procedure is the careful selection of only those events associated with tunnels. While in the case considered here, many seismic events outside of Area 3 have mechanisms with significant implosive and pancake-shape CLVD components, they are likely related to a sudden increase in the depth of failure around stopes. The reduction to two-dimensional geometry in the derivation of Equation (4) is not valid for such excavation geometries, and so we have not attempted to infer the depth of failure increase using it.



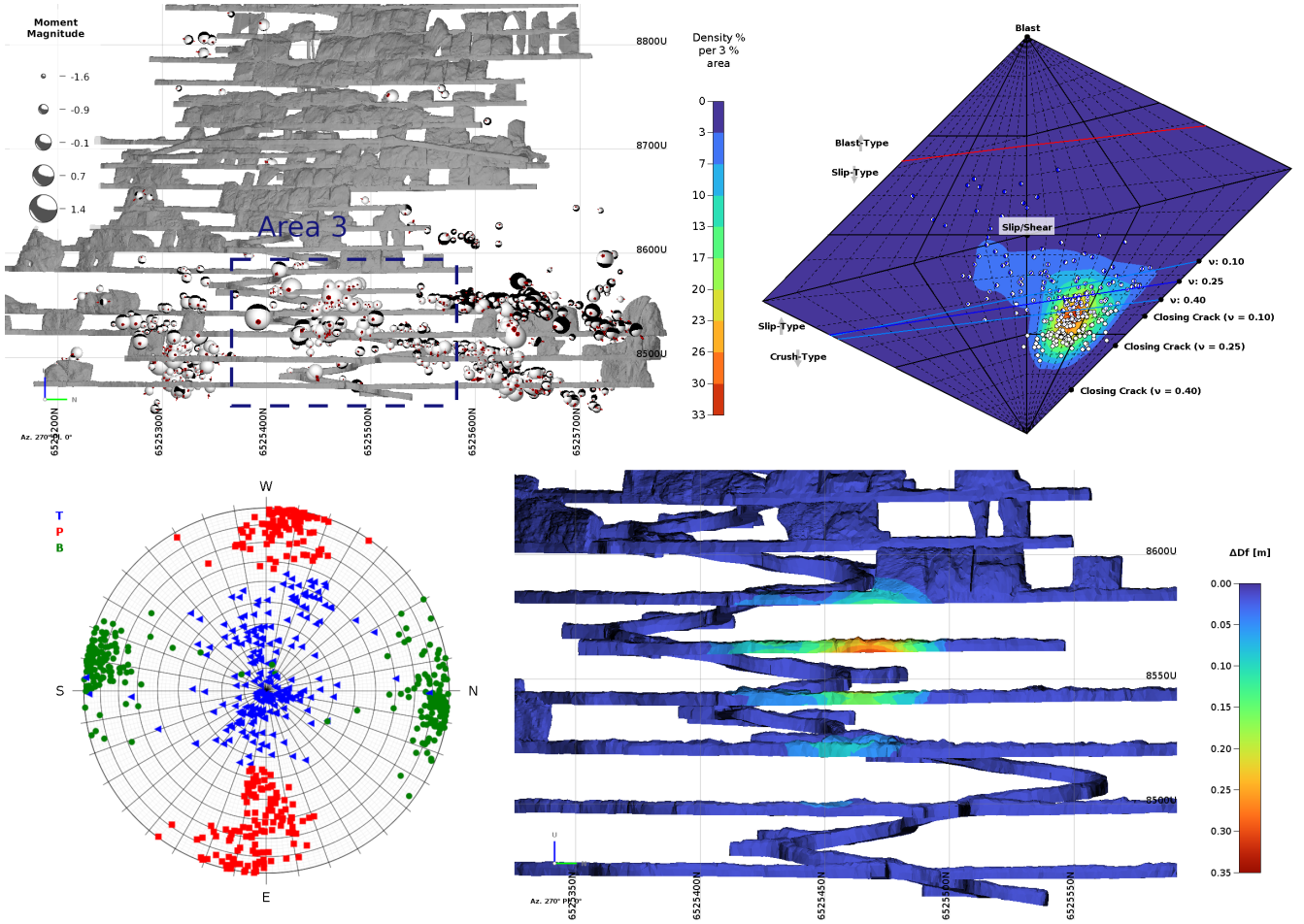


Figure 16: Seismic events recorded from 1 January to 8 June 2019 (*top left*). The visualization of seismic events is the same as in Figure 9. Gray wireframes describe excavations as of the beginning of 2019. The mechanisms of events in Area 3 are visualized in a source-type plot (*top right*) and stereonet of principal axes (*bottom left*). The stereonet is rotated  $90^\circ$  clockwise to match the view in Figure 9. Contours of increase in depth of failure  $\Delta d_f^A$  inferred from seismic events (*bottom right*).

## 5 Discussion

### 5.1 Classification

In the context of underground mining operations, it has been suggested to discriminate between “crush-type” and “slip-type” seismic events [27]; the former being described as an “unstable crushing of volume of rock in close proximity to mining void” and the latter as an “unstable release of shear stress by slip over a planar area (plane of weakness, including ‘intact’ rock).” This discrimination can be achieved by measuring the similarity of a given event to seismic point sources for “ideal” crush- and slip-type events. However, no particular source model is proposed in [27] to describe crush-type events. Given this, we suggest the use of the closing-crack model [6, 4], which is composed of three orthogonal compressional vector dipoles with an amplitude ratio of  $1 : 1 : (1/\nu - 1)$ , for an ideal crush-type event. The closing crack model with a sub-vertically oriented largest dipole has previously been used to describe processes such as near-surface spalling during underground nuclear explosions and massive collapse in mines with sub-horizontally oriented ore bodies. The point sources obtained in Sections 2 and 3 also resemble a closing-crack source with the largest dipole co-oriented with the tunnel’s loading. As this direction is arbitrary in general, it is sensible for any discrimination procedure between crush- and slip-type events

to be orientation invariant. Graphically, this can be achieved by assessing “closeness” to closing-crack and double-couple point sources on source-type plots such as those presented in [34, 35, 11]. For the plots of [11] employed in this paper (see, for example, Table 2, Figures 11 and 16), we have marked the location of closing-crack point sources for three variants of Poisson’s ratio ( $\nu = 0.1, 0.25$ , and  $0.4$ ). Given the proximity of the modelled sources in Sections 2 and 3 (as well as the majority of observed sources in Section 4) to these points, we consider it appropriate to classify them as crush type.

This classification process can be made quantitative through the use of a distance metric to assess the “closeness” of sources. We take the distance between moment tensors  $M$  and  $N$  as the angle  $\omega$  between the vectors  $\mathbf{m} = (m_1, m_2, m_3)$  and  $\mathbf{n} = (n_1, n_2, n_3)$ , where  $m_i$  and  $n_i$  are the  $i$ th largest eigenvalues of  $M$  and  $N$ , respectively; that is,  $\omega = \arccos(\mathbf{m} \cdot \mathbf{n} / \|\mathbf{m}\| \|\mathbf{n}\|)$ . We also extend the classification of [27] by including the category of “blast-type” events, for which the ideal point source represents a combination of three orthogonal extensional vector dipoles of equal amplitude. Using the described metric, the source-type plot of [11] can be separated into three regions by a line of equal proximity to ideal blast- and slip-type sources

$$k = \begin{cases} \frac{T+4}{\sqrt{2/3}T+2(\sqrt{6}+2)} & \text{for } -1 \leq T \leq 0, \\ \frac{T-4}{T-2(\sqrt{6}+2)} & \text{for } 0 \leq T \leq 1, \end{cases}$$

and a line of equal proximity to ideal slip- and crush-type sources

$$k = \begin{cases} -\frac{2(\sqrt{2}q+2-1/\nu)+(q/\sqrt{2}+2-1/\nu)T}{2(\sqrt{2}q+3)+(q/\sqrt{2}+2-1/\nu)T} & \text{for } -1 \leq T \leq 0, \\ -\frac{2(\sqrt{2}q+2-1/\nu)-qT/\sqrt{2}}{2(\sqrt{2}q+3)-qT/\sqrt{2}} & \text{for } 0 \leq T \leq 1, \end{cases}$$

where  $\nu$  is the Poisson’s ratio and  $q = \sqrt{3 + 1/\nu^2 - 2/\nu}$ . These lines are shown on the source-type plots presented in this paper (see, for example, Table 2, Figures 11 and 16). That all the modelled sources in Sections 2 and 3 fall below the line separating slip and crush-type sources quantitatively justifies their being classified as crush-type. The same applies for the majority of real events presented in Section 4.

## 5.2 Interpretation

We note that crush-type sources should not be considered as exotic: there are numerous observations in mines that report source mechanisms with significant implosive components [22, 32, 16]. Although examples from a single mine are presented in Section 4, the authors have observed crush-type sources at a number of other mines. In fact, at some underground mines, seismic events of this type constitute the majority of recorded seismicity (both in terms of number of events and even cumulative seismic moment).

Quite often, seismic data recorded in mines is processed and interpreted assuming a double-couple source model. The nodal planes of the inferred mechanisms are then compared with mapped geological structures (such as faults, contacts of lithological units, etc.) or considered as possible surfaces of shear rupture of intact rock. The results presented in previous sections suggest that such interpretation is not always meaningful. Although the modelled source mechanisms shown in Table 2 have non-zero double-couple components, the corresponding nodal planes do not indicate the presence of slip or shear rupture surfaces. If the sources of seismic events are located close to tunnels (or other excavations, as discussed below) and have crush-type mechanisms, then it can be more useful to attempt interpretation in terms of the model of Equation (3).

## 5.3 Limitations

The numerical modelling presented in Section 2 and the approximations outlined in Section 3 have the following known limitations:

- Tunnels were considered two-dimensionally under the assumption of plane strain, and the extent of failure along the tunnel was taken into account by means of a simple length coefficient  $L_3$  (as discussed previously, this is equivalent to taking a finite slice of an infinite-length tunnel). In reality, damage is not distributed uniformly along the tunnel, and full three-dimensional modelling of this distribution would be preferable. Furthermore, approximation in terms of ellipsoidal cavity expansion rather than the elliptical cavity expansion considered in Section 3 may be more appropriate; this requires further exploration in future work.
- The proposed model is focused on the case of isolated tunnel in homogeneous stress field. However, in mining environments, tunnels are typically surrounded by other excavations (such as caves, stopes and other tunnels), which make the loading conditions softer. This means that the same increment in the depth of failure  $\Delta d_f^A$  for a tunnel may produce different elastic convergence of the surrounding rock mass depending on the proximity to and configuration of other excavations. In this sense, Equation (4) provides the lower-bound estimate of seismic moment  $|\mathbf{M}|$ . It is expected that softer loading conditions (due to the presence of neighboring excavations) will result in larger seismic moment  $|\mathbf{M}|$  for the same  $\Delta d_f^A$ . Analysis of this would be an interesting avenue for future research.

## 5.4 Applications

The suggested source mechanism model of Equation (3) has several applications:

- Forensic analysis of damaging events: If a seismic event locates close to a damaged tunnel, then it makes sense to test the hypothesis that the source of the event and the source of damage are the same. A modelled source mechanism can be determined using Equation (3) and compared with one inverted from recorded seismic waveforms. If these mechanisms have reasonable agreement in terms of scalar moment, direction of principal axis, and source type, then it makes sense to conclude that dynamic stress fracturing around the tunnel was the source of the seismic event. Alternatively, if for example, the modelled scalar moment is smaller than that derived from observation, it implies that the rock fracturing associated with damage is not substantial enough to explain the entire recorded seismic radiation. In such cases, it can be useful to detect “fingerprints” of damage within the recorded waveforms. This can be done by calculating synthetic waveforms for the modelled mechanism (corresponding to damage) and correlating these with high-frequency pulses in the recorded waveforms. If a match is found, then the temporal and spatial relation between the damage and larger-scale deformation of the rockmass (which is responsible for the majority of recorded seismic radiation) can be established.
- Monitoring of deformation of tunnels: Identification of crush-type events around tunnels and interpreting them in terms of Equation (3) makes it possible to quantify the growth of damage zone around tunnels. This can be used in assessing the consumption of capacity of ground support systems installed in tunnels.
- Assessment of dynamic loading to ground support of tunnels: If sources of seismic event in mines are located away from the tunnel of interest, then dynamic loading is assessed in terms of intensity of ground motion (shaking). For seismic sources considered in this work, a better characteristics of loading will be associated with the amount or rate of deformation within the stress-fracturing rock (for example, the amplitude or rate of tangential straining on the perimeter of excavation).
- Other excavations: While the focus of this work has been on events associated with tunnels, the suggested model [described by Equation (3)] can be applied to other types of excavations, such as ore passes, shafts, stopes, or caves, provided that their geometrical characteristics can be approximated by a two-dimensional elliptical cavity. If the shape of excavations is more complex, then Equations (1) or (2) need to be used. The model is also potentially applicable to underground excavations

associated with non-mining applications (for example, nuclear waste storage, hydro-electric stations, etc.). The key requirement in all of these cases is that the seismic wavelengths of interest must be larger than the size of the excavation; for example, at wavelengths of hundreds of meters, the model may be applicable for stopes (dimensions of 20 – 50 m) but not for caves (dimensions of several hundred meters).

## Data and Resources

Permission is required to obtain the data used in Section 4, which are property of the mine. The supplemental material describes the verification tests of the Material Point Method and constitutive relations used for modelling presented in Section 2. Also included are animations showing the dynamics of the sources for Cases 1-6.

## Acknowledgments

The model considered in this work was motivated by the presentations of Prof. Peter Kaiser at Institute of Mine Seismology (IMS) seminars. The advice of Prof. Mark Diederichs and Prof. Peter Kaiser regarding the modelling parameters is highly appreciated. We are thankful to the mine, which provided permission to use their data in Section 4. Gys Basson (IMS) advised and assisted in numerical modelling. Martin Gal (IMS) has helped to validate the expressions presented in Section 5.

## References

- [1] K. Aki and P. Richards. *Quantitative seismology*. University Science Books, 2 edition, 2002.
- [2] G. Backus and M. Mulcahy. Moment tensors and other phenomenological descriptions of seismic sources - I. Continuous displacements. *Geophysical Journal of the Royal Astronomical Society*, 46:341–361, 1976.
- [3] G. Basson, A. P. Bassom, and B. P. Salmon. Simulating mining-induced seismicity using the material point method. *Submitted to Rock Mechanics and Rock Engineering manuscript*, 2021. (under review).
- [4] D. Bowers and W. R. Walter. Discriminating between large mine collapses and explosions using teleseismic P waves. *Pure and Applied Geophysics*, 159:803–830, 2002.
- [5] M. Cai and P. K. Kaiser. *Rockburst phenomena and support characteristics*, volume I in Rockburst Support Reference Book. MIRARCO Laurentian University, 2018. Open access manuscript released 2018; [www.mirarco.org](http://www.mirarco.org).
- [6] S. M. Day and K. L. McLaughlin. Seismic source representations for spall. *Bulletin of the Seismological Society of America*, 81(1):191–201, 1991.
- [7] M. S. Diederichs. The 2003 Canadian Geotechnical Colloquium: Mechanistic interpretation and practical application of damage and spalling prediction criteria for deep tunnelling. *Canadian Geotechnical Journal*, 44(9):1082–1116, 2007.
- [8] P. Fritz. An analytical solution for axisymmetric tunnel problems in elasto-viscoplastic media. *International Journal for Numerical and Analytical Methods in Geomechanics*, 8:325–342, 1984.
- [9] V. Hajiabdolmajid, P. K. Kaiser, and C. D. Martin. Modelling brittle failure of rock. *International Journal of Rock Mechanics and Mining Sciences*, 39(6):731–741, 2002.



- [10] T. C. Hanks and H. Kanamori. A moment magnitude scale. *Journal of Geophysical Research: Solid Earth*, 84(B5):2348–2350, 1979.
- [11] J. A. Hudson, R. G. Pearce, and R. M. Rogers. Source type plot for inversion of the moment tensor. *Journal of Geophysical Research*, 94(B1):765–774, 1989.
- [12] S. Ide. *Treatise on Geophysics*, chapter Slip inversion, pages 193–223. 2007.
- [13] Itasca Consulting Group. *FLAC3D: Fast Lagrangian Analysis of Continua in 3 Dimensions. Theory and background*, 4.0 edition, 2009.
- [14] A. K. Jain. *Fundamentals of digital image processing*. Prentice-Hall, Inc., 1989.
- [15] I. Jassim. *Formulation of a dynamic material point method (MPM) for geomechanical problems*. PhD thesis, Institute of Geotechnical Engineering, University of Stuttgart, 2013.
- [16] J. Julia, A. A. Nyblade, R. Durrheim, L. Linzer, R. Gok, P. Dirks, and W. Walter. Source mechanisms of mine-related seismicity, Savuka mine, South Africa. *Bulletin of the Seismological Society of America*, 99(5):2801–2814, 2009.
- [17] L. M. Kachanov. *Fundamentals of the theory of plasticity*. Dover Publications, 2004.
- [18] P. K. Kaiser and M. Cai. *Rock support to mitigate rockburst damage caused by dynamic excavation failure*, volume II in Rockburst Support Reference Book. MIRARCO Laurentian University, 2021. Draft manuscript available from Geo-Kaiser.ca.
- [19] D. Malovichko. Description of seismic sources in underground mines: Theory. *Bulletin of the Seismological Society of America*, 110, 2020.
- [20] D. Maugis. Stresses and displacements around cracks and elliptical cavities: Exact solutions. *Engineering Fracture Mechanics*, 43:217–255, 1992.
- [21] A. McGarr. An implosive component in the seismic moment tensor of a mining-induced tremor. *Geophysical Research Letters*, 19(15):1579–1582, 1992.
- [22] A. McGarr. Moment tensors of ten Witwatersrand tremors. *Pure and Applied Geophysics*, 139(3/4):781–800, 1992.
- [23] J. A. Nairn. Material point method calculations with explicit cracks. *Computer Modeling in Engineering and Sciences*, 4(6):649–664, 2003.
- [24] A. Olson and R. Apsel. Finite faults and inverse theory with applications to the 1979 Imperial Valley earthquake. *Bulletin of the Seismological Society of America*, 72:1969–2001, 1982.
- [25] W. D. Ortlepp. *Rock fracture and rockbursts - An illustrative study*. SAIMM, 1997.
- [26] M. A. Perras and M. S. Diederichs. Predicting excavation damage zone depths in brittle rocks. *Journal of Rock Mechanics and Geotechnical Engineering*, 8(1):60–74, 2016.
- [27] J. A. Ryder. Excess shear stress in the assessment of geologically hazardous situations. *Journal of the Southern African Institute of Mining and Metallurgy*, 88(1):27–39, 1988.
- [28] H. Si. TetGen, a Delaunay-based quality tetrahedral mesh generator. *ACM Transactions on Mathematical Software (TOMS)*, 41(2):1–36, 2015.

- [29] J. Sileny, I. Psencik, and R. P. Young. Point-source inversion neglecting a nearby free surface: simulation of the Underground Research Laboratory, Canada. *Geophysical Journal International*, 146:171–180, 2001.
- [30] P. G. Silver and T. H. Jordan. Optimal estimation of scalar seismic moment. *Geophysical Journal of the Royal Astronomical Society*, 70(3):755–787, 1982.
- [31] E. S. Sørensen, J. Clausen, and L. Damkilde. Finite element implementation of the Hoek-Brown material model with general strain softening behavior. *International Journal of Rock Mechanics and Mining Sciences*, 78:163–174, 2015.
- [32] M. C. Stickney and K. F. Sprenke. Seismic events with implosional focal mechanisms in the Coeur d’Alene Mining District, northern Idaho. *Journal of Geophysical Research*, 98(B4):6523–6528, 1993.
- [33] Y. Takei and M. Kumazawa. Why have the single force and torque been excluded from seismic source models? *Geophysical Journal International*, 118:20–30, 1994.
- [34] W. Tape and C. Tape. A geometric comparison of source-type plots for moment tensors. *Geophysical Journal International*, 190:499–510, 2012.
- [35] V. Vavrycuk. Moment tensor decompositions revisited. *Journal of Seismology*, 19:231–252, 2015.
- [36] B. Wang, P. J. Vardon, M. A. Hicks, and Z. Chen. Development of an implicit material point method for geotechnical applications. *Computers and Geotechnics*, 71:159–167, 2016.

# Appendices

## A Details of modelling of seismic sources

Following the procedure of the verification tests available in the supplemental material, our MPM simulations employ grids based on tetrahedral meshes produced using TETGEN [28]. An example of a simplified (coarse) version of the mesh used for Cases 1-4 and 6 is shown in Figure 17. The meshes are 100 m diameter square plates with a thickness of 5 m composed of a single layer of tetrahedra whose vertices lie on contours that, with allowances for boundary geometry, are concentric to the profile of the tunnel itself (this reduction to what is essentially a two-dimensional setup follows the discussion of Section 2.2). In practice, 96 vertices lie on each of these contours (rather than the 48 shown in Figure 17) and are separated by equal angles as measured from the center of the tunnel. The radial distance between adjacent contours is approximately equal to the spacing of vertices in the smaller contour, making the mesh increasingly coarse away from the tunnel.

Each cell (tetrahedron) is populated with a single particle. The initial stress of these particles is set according to case-varying loading described in Section 2.2 [stress in the direction of the tunnel is set to  $\nu(\sigma_{\max} + \sigma_{\min})$  to satisfy the plane strain assumption]. Fixed stress conditions are applied at the top, bottom, east, and west boundaries; fixed normal displacement (roller) conditions are applied at the north and south boundaries.

As noted in Section 2.2, a CWFS material is used. Brittle failure at low confinement is implemented using an elastic-brittle-plastic Mohr-Coulomb constitutive relation with tension cutoff based on the formulation of [13]. Strain hardening at high confinement is implemented based on the strain-softening Hoek-Brown material constitutive model detailed in [31]. Verification of these two constitutive relations can be found in the supplemental material.

The initial simulation is performed quasi-statically using damping as described in [13, 36]. Expansion of the failed region is simulated dynamically by removing damping within a 50 m of the tunnel’s center

(we preserve damping near the boundaries to limit unwanted reflections) prior to applying one of the perturbations outlined in Section 2.2.

Calculating the surface integrals in Subsection 2.3 requires values of displacement and traction at faces of the tetrahedral mesh. In the case of displacement, this is achieved by first mapping particle displacements to the nodes of their containing cells (tetrahedra) via the shape function. The displacement of any given face is then taken to be the average of the displacement of its constituent nodes. Similarly, stress at faces is determined in the same way, allowing traction to be obtained using the faces' normal vectors.

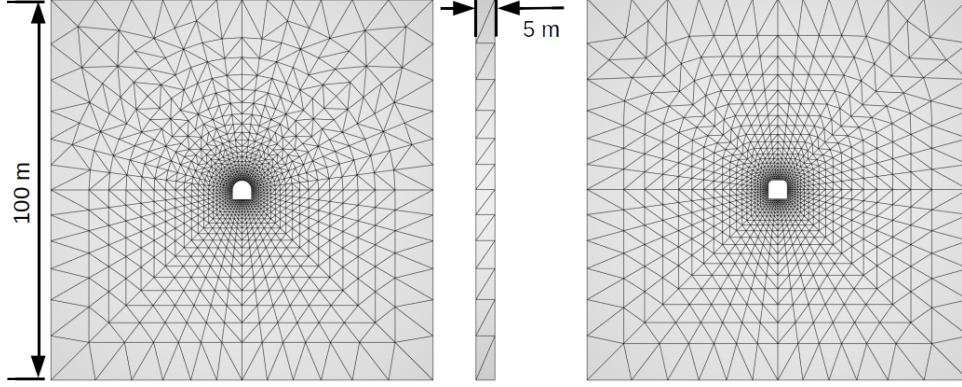


Figure 17: North views of a simplified version of the tetrahedral mesh used for Cases 1-4, and 6 (*left*) and for Case 5 (*right*). East view is shown between them (*middle*).

Figures 18 to 23 show details of the source mechanism calculations for the five modelled cases:

- The top row shows plots matching those presented in the bottom row of Figure 4 for Case 3. The left plot shows the inputs to Equation (1): differential displacement  $\Delta \mathbf{u}$  and traction  $\Delta \mathbf{T}$  along a surface  $S$  in the elastic region, which is contoured in black. The right plot shows the inputs to Equation (2): differential plastic strain  $\Delta \epsilon^p$  and displacement  $\Delta \mathbf{u}$  along the tunnel surface  $\Sigma$ .
- The bottom left plot matches that presented on the right of Figure 6 for Case 3. Pre- and post-expansion approximating ellipses are shown along with  $\Delta \mathbf{u}$  and  $\Delta \mathbf{T}$  along  $S$ .
- The bottom right plot shows the relative invariance in the surface  $S$  selected on the Kirchhoff-type source mechanism calculated from Equation (1). In particular, it shows the variation in the scalar moments  $|\mathbf{M}^T + \mathbf{M}^U|$ ,  $|\mathbf{M}^U|$ , and  $|\mathbf{M}^T|$  for surfaces of varying diameter. The dashed vertical line marks the surface diameter of 15 m used in calculating the mechanisms presented in Sections 2 and 3.

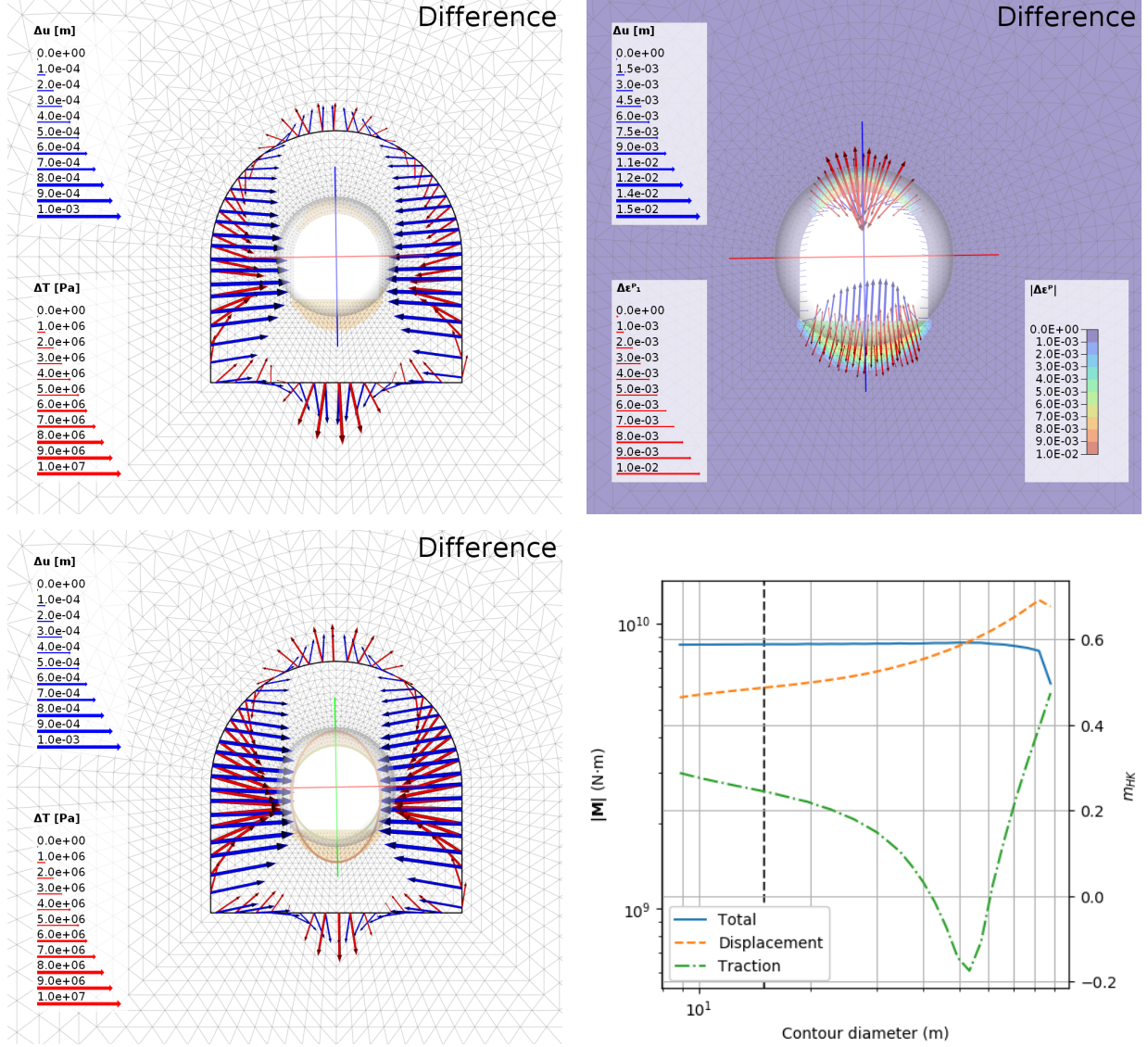


Figure 18: Summaries for Case 1 (horizontal loading, stress increase, failure in the roof and floor) of Kirchhoff (*top left*), adjusted conventional (*top right*), and elliptical (*bottom left*) moment tensor calculations. Demonstration of contour invariance for Kirchhoff-type calculation (*bottom right*). See text for more details.



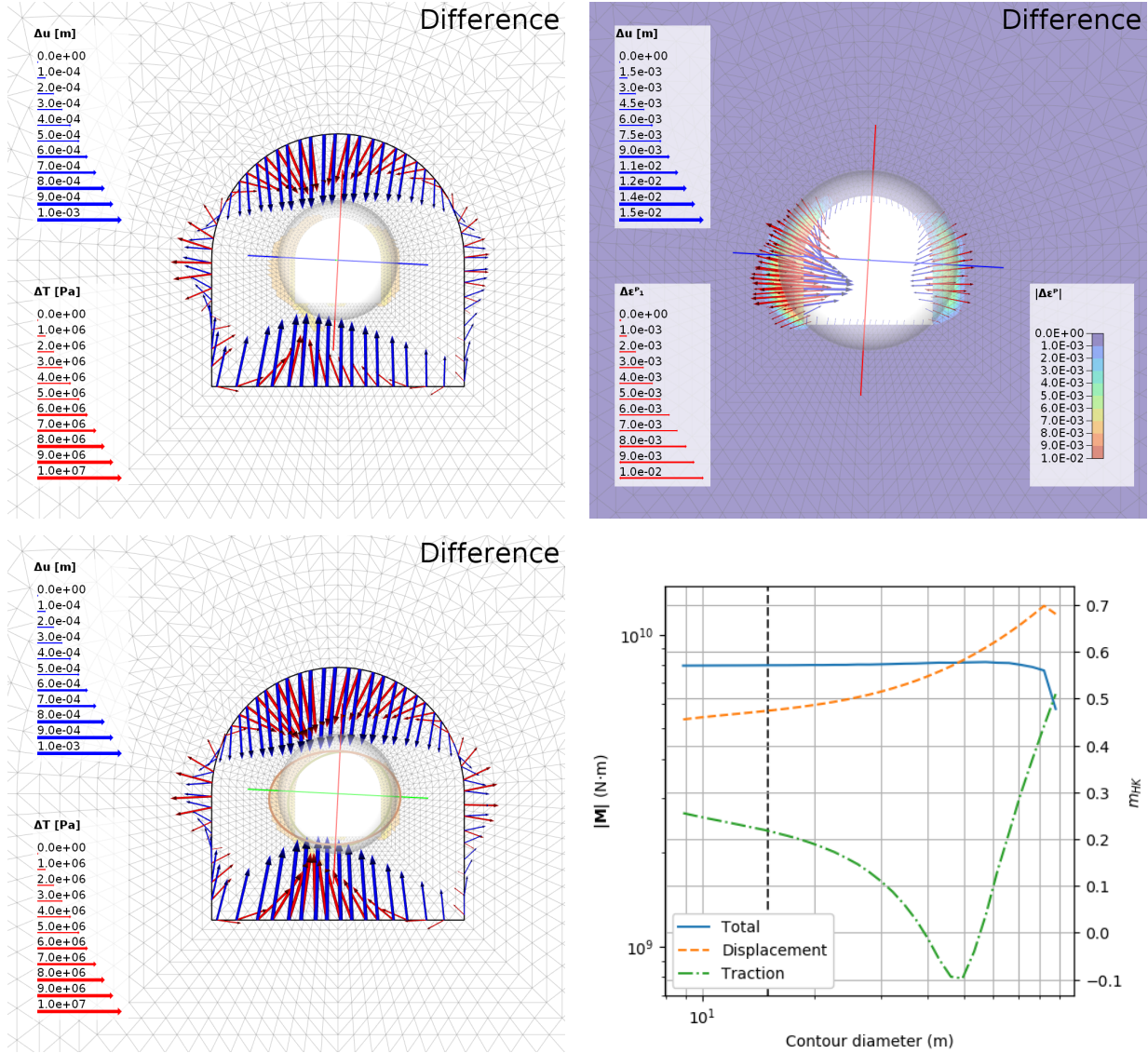


Figure 19: Summaries for Case 2 (vertical loading, stress increase, failure in the walls) of Kirchhoff (*top left*), adjusted conventional (*top right*), and elliptical (*bottom left*) moment tensor calculations. Demonstration of contour invariance for Kirchhoff-type calculation (*bottom right*). See text for more details.

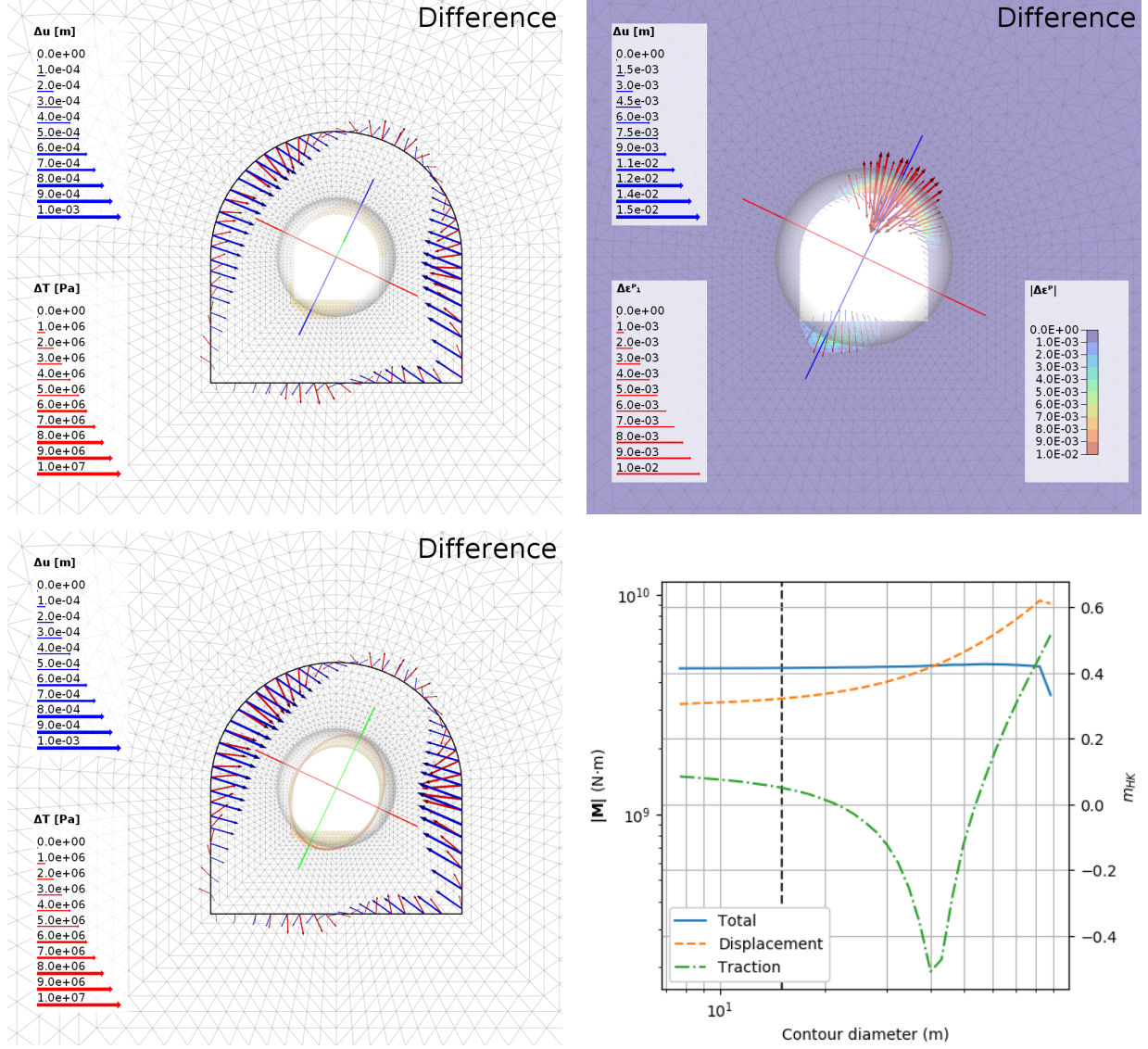


Figure 20: Summaries for Case 3 (eastward plunging loading, stress increase, failure in the eastern shoulder and western bottom corner) of Kirchhoff (*top left*), adjusted conventional (*top right*), and elliptical (*bottom left*) moment tensor calculations. Demonstration of contour invariance for Kirchhoff-type calculation (*bottom right*). See text for more details.

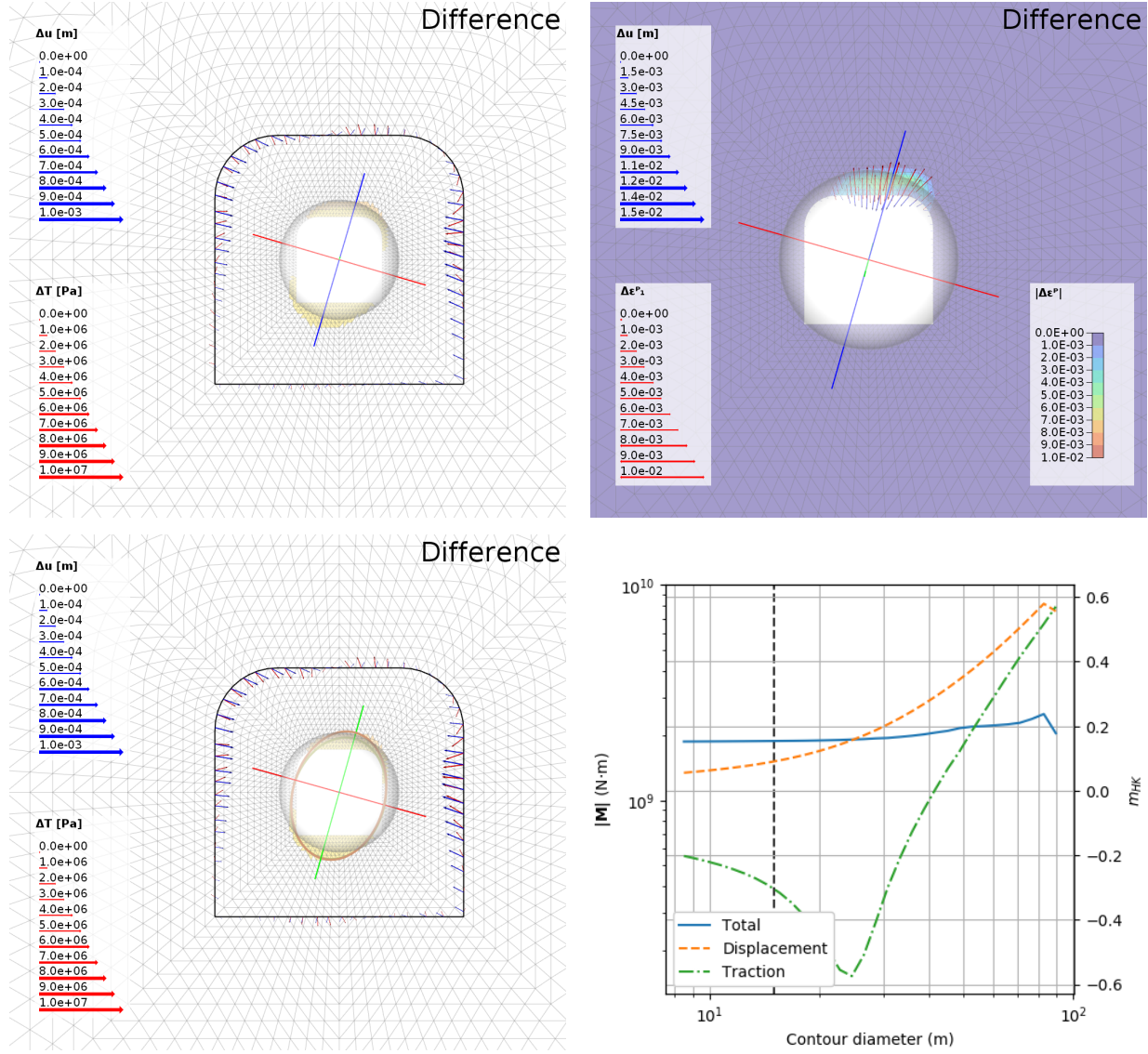


Figure 21: Summaries for Case 4 (eastward plunging loading, stress increase, different profile, failure in the eastern shoulder) of Kirchhoff (*top left*), adjusted conventional (*top right*), and elliptical (*bottom left*) moment tensor calculations. Demonstration of contour invariance for Kirchhoff-type calculation (*bottom right*). See text for more details.



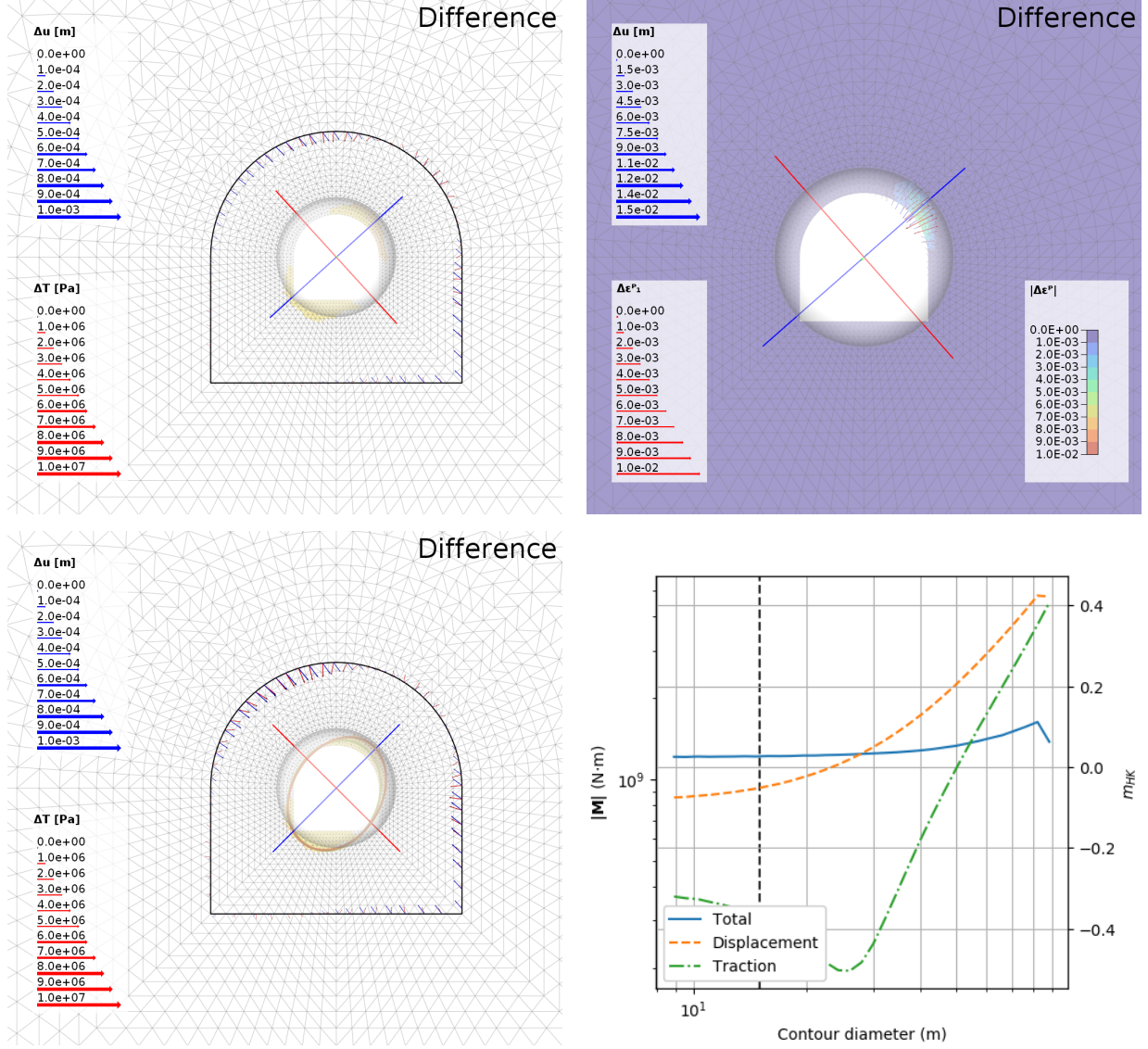


Figure 22: Summaries for Case 5 (eastward plunging loading, stress increase, weaker material, failure in the eastern corner) of Kirchhoff (*top left*), adjusted conventional (*top right*), and elliptical (*bottom left*) moment tensor calculations. Demonstration of contour invariance for Kirchhoff-type calculation (*bottom right*). See text for more details.



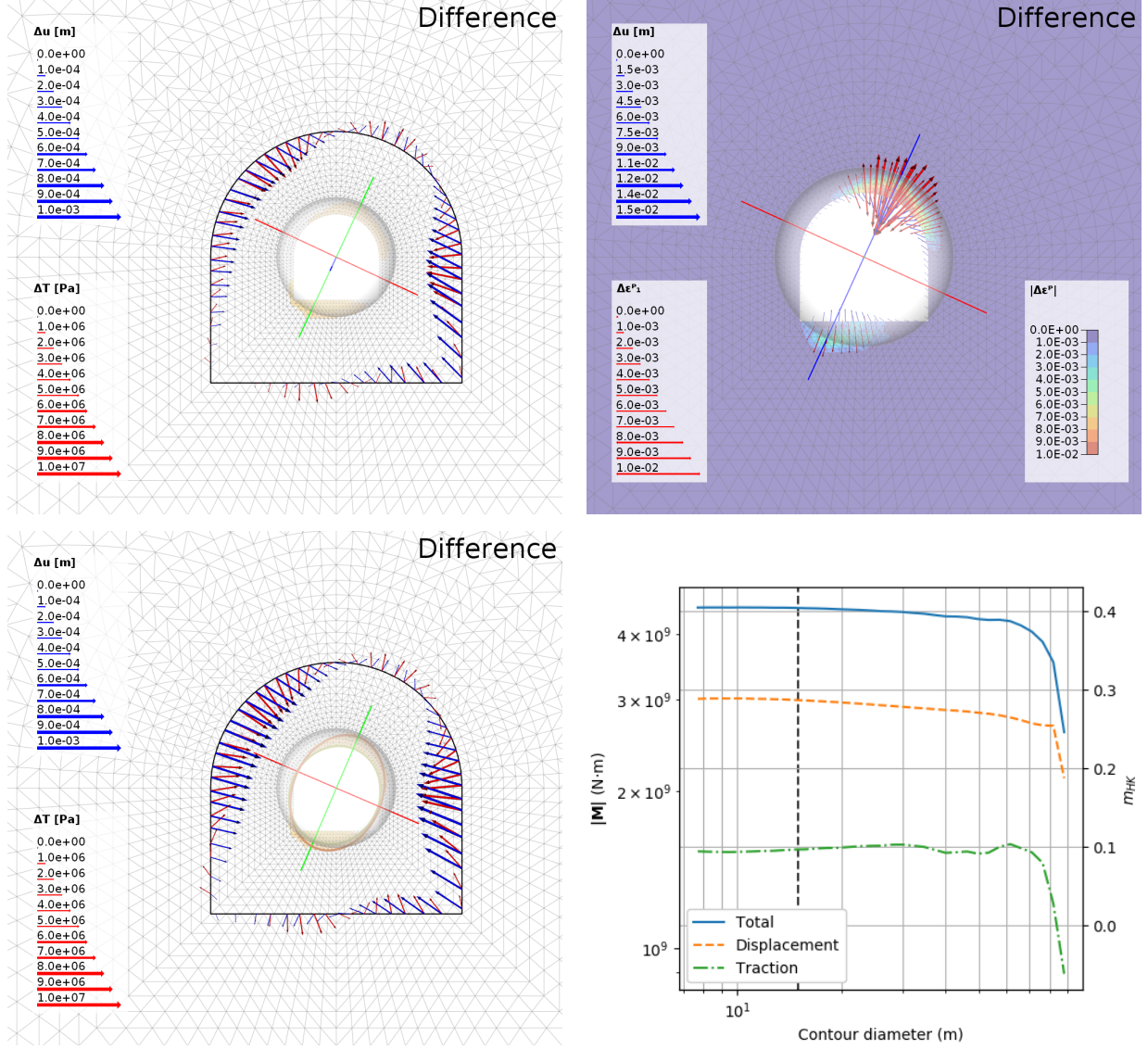


Figure 23: Summaries for Case 6 (eastward plunging loading, stress wave, failure in the eastern shoulder and western bottom corner) of Kirchhoff (*top left*), adjusted conventional (*top right*), and elliptical (*bottom left*) moment tensor calculations. Demonstration of contour invariance for Kirchhoff-type calculation (*bottom right*). See text for more details.

## B Transformations of Equation (1) for an expanding elliptical cavity

When applied to the traction-free surface of the expanded elliptical cavity  $S_2$ , Equation (1) has the form

$$M_{ij} = - \iint_{S_2} \left\{ T_i^{(\text{before})}(\mathbf{x})(x_j - x_j^{(0)}) + c_{ijkl}(\mathbf{x}) \left[ u_k^{(\text{after})}(\mathbf{x}) - u_k^{(\text{before})}(\mathbf{x}) \right] n_l(\mathbf{x}) \right\} dS(\mathbf{x}). \quad (6)$$

A simple analytical expression is known for the displacement  $\mathbf{u}^{(\text{after})}$  on  $S_2$  [20], and integration of that component is relatively straightforward. Expressions for  $\mathbf{T}^{(\text{before})}$  and  $\mathbf{u}^{(\text{before})}$  on  $S_2$  are also available, but their increased complexity makes their integration less straightforward. In this section, we demonstrate a procedure for transforming Equation 6 into a form that makes this integration possible. In the derivation of this transformed expression, we will deal with the deformation and stress fields of the pre-expansion state only, so to simplify notation, we will omit “before” superscripts (that is,  $\boldsymbol{\sigma} \equiv \boldsymbol{\sigma}^{(\text{before})}$ ,  $\mathbf{u} \equiv \mathbf{u}^{(\text{before})}$ , etc.).

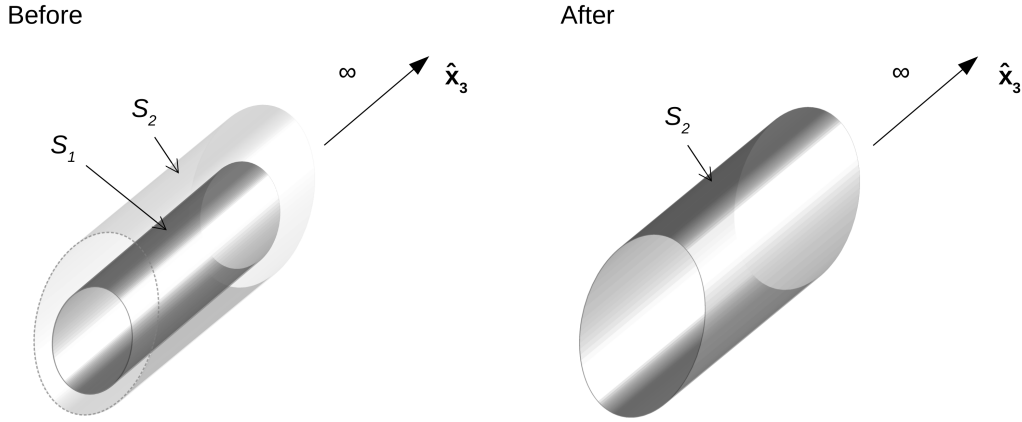


Figure 24: Before (*left*) and after (*right*) the expansion of an infinite extent elliptical cavity oriented in the direction  $\hat{\mathbf{x}}_3$ . Only a limited section is shown and used in the source mechanism calculations. The pre and post-expansion surfaces  $S_1$  and  $S_2$  are shown in dark gray in their respective plots ( $S_2$  is also superimposed on the pre-expansion  $S_1$  to indicate their relative position). Plane strain is assumed in both cases.

Taking  $\hat{\mathbf{x}}_3$  to be oriented along the cavity’s axis as shown in Figure 24, the plane strain condition dictates that displacement in this direction is zero; that is,  $u_3(\mathbf{x}) = 0$ . It also implies that  $\sigma_{13}(\mathbf{x}) = \sigma_{23}(\mathbf{x}) = \sigma_{31}(\mathbf{x}) = \sigma_{32}(\mathbf{x}) = 0$  and  $\sigma_{33}(\mathbf{x}) = \nu[\sigma_{11}(\mathbf{x}) + \sigma_{22}(\mathbf{x})]$ , where  $\nu$  is Poisson’s ratio. Consider the toroidal volume  $V$  confined by the surfaces  $S_1$  and  $S_2$  radially, and by the surfaces  $S_{3+}$  and  $S_{3-}$  in the direction of  $\hat{\mathbf{x}}_3$ . At equilibrium,

$$\frac{\partial \sigma_{im}(\mathbf{x})}{\partial x_m} = 0$$

for all  $\mathbf{x} \in V$ . Multiplying this by the  $j$ th component of  $\mathbf{x}$  relative to an arbitrary location  $\mathbf{x}^{(0)}$  gives

$$\frac{\partial \sigma_{im}(\mathbf{x})}{\partial x_m} (x_j - x_j^{(0)}) = 0.$$

Following integration over  $V$ , applying the product rule, and the divergence theorem, this becomes

$$\iint_{\partial V} T_i^V(\mathbf{x})(x_j - x_j^{(0)}) dS(\mathbf{x}) - \iiint_V \sigma_{ij}(\mathbf{x}) dV(\mathbf{x}) = 0,$$

where stress is presented in terms of the traction  $T_i^V(\mathbf{x}) = \sigma_{im}(\mathbf{x})n_m^V(\mathbf{x})$ , and the surface  $\partial V$  is composed of  $S_1$ ,  $S_2$ ,  $S_{3+}$ , and  $S_{3-}$ . Note that this normal vector  $\mathbf{n}^V$  is oriented outwards from the volume  $V$ , meaning that it is not the same as  $\mathbf{n}$  in Equation (6):  $\mathbf{n}^V(\mathbf{x}) = \mathbf{n}(\mathbf{x})$  for  $\mathbf{x} \in S_2$  but  $\mathbf{n}^V(\mathbf{x}) = -\mathbf{n}(\mathbf{x})$  for  $\mathbf{x} \in S_1$ . Substituting  $\sigma_{ij}(\mathbf{x}) = c_{ijkl}\partial u_k(\mathbf{x})/\partial x_l$  and applying the divergence theorem to the second integral yields<sup>1</sup>

$$\iint_{\partial V} T_i^V(\mathbf{x})(x_j - x_j^{(0)})dS(\mathbf{x}) - \iint_{\partial V} c_{ijkl}u_k(\mathbf{x})n_l^V(\mathbf{x})dS(\mathbf{x}) = 0.$$

For  $i = 1$  or  $2$ , we have

$$\iint_{S_2} T_i^V(\mathbf{x})(x_j - x_j^{(0)})dS(\mathbf{x}) - \iint_{S_2} c_{ijkl}u_k(\mathbf{x})n_l^V(\mathbf{x})dS(\mathbf{x}) = \iint_{S_1} c_{ijkl}u_k(\mathbf{x})n_l^V(\mathbf{x})dS(\mathbf{x}),$$

and for  $i = 3$ , we have

$$\iint_{S_{3+} \cup S_{3-}} T_3^V(\mathbf{x})(x_3 - x_3^{(0)})dS(\mathbf{x}) = \iint_{S_1 \cup S_2} \lambda[u_1(\mathbf{x})n_1^V(\mathbf{x}) + u_2(\mathbf{x})n_2^V(\mathbf{x})]dS(\mathbf{x}).$$

In terms of notations used in Equation (6), these equations become

$$- \iint_{S_2} T_i^{(\text{before})}(\mathbf{x})(x_j - x_j^{(0)})dS(\mathbf{x}) + \iint_{S_2} c_{ijkl}u_k^{(\text{before})}(\mathbf{x})n_l(\mathbf{x})dS(\mathbf{x}) = \iint_{S_1} c_{ijkl}u_k^{(\text{before})}(\mathbf{x})n_l(\mathbf{x})dS(\mathbf{x})$$

and

$$\iint_{S_{3+} \cup S_{3-}} T_3^{(\text{before})}(\mathbf{x})(x_3 - x_3^{(0)})dS(\mathbf{x}) + \iint_{S_1} \lambda[u_1^{(\text{before})}(\mathbf{x})n_1(\mathbf{x}) + u_2^{(\text{before})}(\mathbf{x})n_2(\mathbf{x})]dS(\mathbf{x}) = \iint_{S_2} \lambda[u_1^{(\text{before})}(\mathbf{x})n_1(\mathbf{x}) + u_2^{(\text{before})}(\mathbf{x})n_2(\mathbf{x})]dS(\mathbf{x}),$$

respectively. These equations allow Equation (6) to be re-expressed as

$$\left\{ \begin{array}{ll} M_{ij} = \iint_{S_1} c_{ijkl}(\mathbf{x})u_k^{(\text{before})}(\mathbf{x})n_l(\mathbf{x})dS(\mathbf{x}) - \iint_{S_2} c_{ijkl}(\mathbf{x})u_k^{(\text{after})}(\mathbf{x})n_l(\mathbf{x})dS(\mathbf{x}) & \text{if } i, j = 1 \text{ or } 2, \\ M_{33} = \iint_{S_1} \lambda[u_1^{(\text{before})}(\mathbf{x})n_1(\mathbf{x}) + u_2^{(\text{before})}(\mathbf{x})n_2(\mathbf{x})]dS(\mathbf{x}) + \\ \quad \iint_{S_{3+} \cup S_{3-}} T_3^{(\text{before})}(\mathbf{x})(x_3 - x_3^{(0)})dS(\mathbf{x}) - \\ \quad \iint_{S_2} \lambda[u_1^{(\text{after})}(\mathbf{x})n_1(\mathbf{x}) + u_2^{(\text{after})}(\mathbf{x})n_2(\mathbf{x})]dS(\mathbf{x}) & , \\ M_{ij} = 0 & \text{otherwise.} \end{array} \right. \quad (7)$$

The next step is to express Equation (7) in terms of the characteristics of loading and the geometric parameters of the ellipses, which will require two approximations. The first of these is to assume that the minor semi-axes of both ellipses are aligned with the direction of maximum in-plane compressive stress (marked as “Load” in Figure 5). This is a reasonable assumption as stress concentration and damage

<sup>1</sup>For example,  $\iiint_V \partial u_1(\mathbf{x})/\partial x_2 dV(\mathbf{x}) = \iint_{\partial V} u_1(\mathbf{x})n_2(\mathbf{x})dS(\mathbf{x})$  is obtained by applying the divergence theorem to the vector field  $(0, u_1(\mathbf{x}), 0)$ . This equation also justifies the invariance of Kirchhoff-type definition for moment tensor of Equation (1) in regards to selection of the integration surface  $S$  (taking the effect of side surfaces  $S_{3+}$  and  $S_{3-}$  into account).

tend to occur in this direction as illustrated by the modelling of Section 2. The second approximation is to neglect the traction term in the expression for  $M_{33}$ , allowing the source mechanism to be defined entirely by displacements on the original and final cavities. Denoting the major and minor semi-axes of the original ellipse as  $a^{(\text{before})}$  and  $b^{(\text{before})}$ , respectively, and those of the final ellipse as  $a^{(\text{after})}$  and  $b^{(\text{after})}$ , respectively, the components of the moment tensor in a coordinate system with  $\hat{\mathbf{x}}_1$  and  $\hat{\mathbf{x}}_2$  oriented along the major and minor semi-axes are

$$M_{ij} = \begin{cases} K \left[ \frac{\nu}{1-2\nu} + \frac{1-\nu}{1-2\nu} \frac{1}{k_\sigma} \frac{b}{a} \frac{\Delta b}{\Delta a} - \frac{k_\sigma-1}{4k_\sigma} \left( \frac{b}{a} + \frac{\Delta b}{\Delta a} \right) + \frac{\nu}{1-2\nu} \frac{1}{2} \frac{\Delta a}{a} - \frac{k_\sigma-1}{4k_\sigma} \frac{\Delta b}{a} + \frac{1-\nu}{1-2\nu} \frac{1}{2k_\sigma} \frac{\Delta b}{a} \frac{\Delta b}{\Delta a} \right] & \text{if } i, j = 1, \\ K \left[ \frac{1-\nu}{1-2\nu} + \frac{\nu}{1-2\nu} \frac{1}{k_\sigma} \frac{b}{a} \frac{\Delta b}{\Delta a} + \frac{k_\sigma-1}{4k_\sigma} \left( \frac{b}{a} + \frac{\Delta b}{\Delta a} \right) + \frac{1-\nu}{1-2\nu} \frac{1}{2} \frac{\Delta a}{a} + \frac{k_\sigma-1}{4k_\sigma} \frac{\Delta b}{a} + \frac{\nu}{1-2\nu} \frac{1}{2k_\sigma} \frac{\Delta b}{a} \frac{\Delta b}{\Delta a} \right] & \text{if } i, j = 2, \\ K \frac{\nu}{1-2\nu} \left[ 1 + \frac{1}{k_\sigma} \frac{b}{a} \frac{\Delta b}{\Delta a} + \frac{1}{2} \frac{\Delta a}{a} + \frac{1}{2k_\sigma} \frac{\Delta b}{a} \frac{\Delta b}{\Delta a} \right] & \text{if } i, j = 3, \\ 0 & \text{otherwise,} \end{cases} \quad (8)$$

where  $K = 4\pi k_\sigma \sigma (1 - \nu) a \Delta a L$ ,  $\sigma$  is the loading along the major semi-axis,  $k_\sigma \sigma$  is the loading along the minor semi-axis,  $\nu$  is the rockmass' Poisson's ratio,  $L$  is the tunnel's extent in  $\hat{\mathbf{x}}_3$ ,  $\Delta a \equiv a^{(\text{after})} - a^{(\text{before})}$ , and  $\Delta b \equiv b^{(\text{after})} - b^{(\text{before})}$ .